Bol. Soc. Esp. Mat. Apl. n°30(2004), 49–102

Numerical Simulation of Fluid Flow with Moving and Free Boundaries

L.H. Juárez[1], R. Glowinski[2] and T.W. Pan[2]

[1]Departamento de Matemáticas, Universidad Autónoma Metropolitana–I, México D.F.
[2]Department of Mathematics, University of Houston, Houston Texas.

hect@xanum.uam.mx, roland@math.uh.edu, pan@math.uh.edu

Abstract

The main goal of this article is to discuss the numerical simulation of incompressible viscous fluid flow with moving and free boundaries. The case of flow with moving boundaries include the direct numerical simulation of moving rigid bodies of various shapes in viscous fluids. The case of flow with free boundaries include the numerical simulation of a viscous fluid flow with a free capillary surface. The main components of the methodology applied to the solution of these problems are: (i) space approximation by finite element methods, (ii) time integration by operator–splitting, (iii) treatment of advection by a wave–like equation method, (iv) treatment of the incompressibility by L^2 or H^1–projection methods, and (v) Lagrange multiplier/fictitious domain methods in the case of flow with moving rigid bodies. We present the results of various numerical experiments, including the sedimentation of rigid bodies, the motion of hydrodynamic pendula, and capillary free–surface flow.

Key words: *Navier–Stokes equations, finite element methods, operator splitting, fictitious domain method, distributed Lagrange multiplier, free surface flow, particulate flow.*

AMS subject classifications: *76D05, 76M10, 35R35, 70F99.*

1 Introduction

In this article we discuss a methodology that allows the direct numerical simulation of incompressible viscous fluid flow with moving or free boundaries. This is done by an (almost) unified approach for the computational treatment of this type of problems. The methodology that we advocate to address the numerical solution of these problems relies on the combination of:

Fecha de recepción: 19/10/04

- Finite element methods for the space approximation to take advantage of existing variational formulations.
- Operator–splitting for time integration to decouple the numerical and physical difficulties, and treat optimally, the various operators present in the model.
- Volume distributed Lagrange multiplier based fictitious domain methods to solve the flow in a fixed space region, in the case of flow with moving rigid boundaries.
- Wave–like equation methods for the treatment of advection.
- L^2 or H^1–projection methods for the treatment of incompressibility.

The present article reviews methods and results discussed in references [21], [22], [23], [30], [38], [39], [40], [41]. In Section 2 we apply the methodology to the numerical simulation of fluid flow with moving boundaries. In Section 3 we apply the methodology to the numerical simulation of viscous fluid flow with free boundaries. In Sections 4–8 we present some numerical results including the sedimentation of rigid bodies in an incompressible viscous fluid, flow past moving rigid bodies, the motion of hydrodynamic pendula, and flow with a free surface.

2 Fluid flow with moving boundaries

For more than one decade the direct numerical simulation of *particulate flow* has been a center of attention for many researchers. This fast growing field of investigations has produced several different numerical solvers, often called *particle movers* (see [26] for a review). One of these particle movers is the so called *distributed Lagrange multiplier/fictitious domain* or DLM particle mover. This method has been successfully applied to the numerical solution of various different problems, including the simulation of sedimentation and fluidization of rigid particles in two and three dimensions, flow past rigid bodies, and the motion of hydrodynamic pendula (see above references). Other applications may include the investigation of micro–structure in flowing suspensions, slurry transport and hydraulic fracturing. For these problems the flow is modeled by the Navier–Stokes equations, while the motion of the bodies is modeled by the Newton–Euler equations. These equations are coupled through the no–slip condition on the particle boundaries, as well as the hydrodynamic forces and torques which appear in the equations of rigid–body motion. A key feature of the method is that the interaction between the fluid and the rigid bodies is implicitly modeled by a global variational formulation of the virtual power type, so that the hydrodynamical forces and torques are not computed explicitly during the simulations. The distributed Lagrange multiplier/fictitious domain method consists in filling the moving bodies by the surrounding fluid and enforcing the fluid flow as a rigid body motion on the region originally occupied

by the rigid bodies. Thus a fixed grid can be used for the entire flow simulation, eliminating the need for repeated re–meshing and projection. Then the rigid body constraint is relaxed by using distributed Lagrange multipliers to obtain a flow problem in the entire region. The role of these Lagrange multipliers is to enforce the rigidity inside the regions occupied by the bodies by matching the velocity fields of two continua, namely the fluid and the rigid bodies. To prevent overlapping of the rigid bodies, a *short range repulsive force* is introduced so that when the distance between two particles is less than a given size (usually the mesh size), this repulsive force is activated. The solution method of the resulting equations uses *finite element* discretizations in space and *operator splitting* for time integration. This methodology is applied to the numerical simulation of the sedimentation of rigid bodies in viscous incompressible fluids, flow past rigid bodies and the motion of hydrodynamic pendula. Two finite element approximations have been used to solve these problems: the Bercovier–Pironneau's [8], and the Taylor–Hood's [69].

2.1 A Fluid–particle interaction model and its global variational formulation

Let $\Omega \subset \mathbb{R}^d$ $(d = 2, 3)$ be a space region, with boundary Γ, filled with an *incompressible viscous fluid* of density ρ_f; we suppose that Ω contains J moving rigid bodies $B_1,\ B_2, ..., B_J$ (see Figure 1 for a particular case where $d = 2$ and $J = 4$). We denote by $\mathbf{n}$ the unit normal vector on the boundary of $\Omega_f = \Omega \setminus \cup_{j=1}^{J} \overline{B}_j$, pointing outward to the fluid region. Assuming that the only external force acting on the mixture is *gravity* (denoted by $\mathbf{g}$), then, between *collisions*, the *fluid flow* is modeled by the following *Navier–Stokes equations*

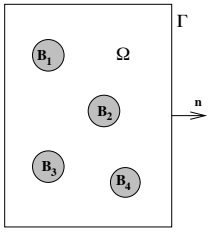

Figure 1: An example of two–dimensional flow region with four rigid bodies.

$$\rho_f \left[\frac{\partial \mathbf{u}}{\partial t} + (\mathbf{u} \cdot \boldsymbol{\nabla})\mathbf{u} \right] = \rho_f \, \mathbf{g} + \boldsymbol{\nabla} \cdot \boldsymbol{\sigma} \ \text{ in } \ \Omega_f(t), \tag{1}$$

$$\boldsymbol{\nabla} \cdot \mathbf{u} = 0 \ \text{ in } \ \Omega_f(t), \tag{2}$$

$$\mathbf{u}(\mathbf{x}, 0) = \mathbf{u}_0(\mathbf{x}), \ \forall \mathbf{x} \in \Omega_f(0) \ \ (\text{with } \ \boldsymbol{\nabla} \cdot \mathbf{u}_0 = 0), \tag{3}$$

where $\mathbf{u}$ denotes the velocity of the fluid, $\boldsymbol{\sigma} = \boldsymbol{\tau} - p\mathbf{I}$ is the *stress–tensor*, with $\boldsymbol{\tau} = \mu \left[\boldsymbol{\nabla}\mathbf{u} + (\boldsymbol{\nabla}\mathbf{u})^t \right]$ for a *Newtonian fluid* with viscosity μ. The above

equations are complemented by the following *boundary conditions*:

$$\mathbf{u} = \mathbf{g}_0 \quad \text{on} \quad \Gamma, \tag{4}$$

$$\mathbf{u}(\mathbf{x},t) = \mathbf{V}_j(t) + \boldsymbol{\omega}_j(t) \times \overrightarrow{\mathbf{G}_j(t)\mathbf{x}}, \ \forall \mathbf{x} \in \partial B_j(t), \quad j = 1, ..., J. \tag{5}$$

In (5) $\mathbf{V}_j$ and $\boldsymbol{\omega}_j$ denote the *velocity of the center of mass* $\mathbf{G}_j$ and the *angular velocity* of the j^{th} body, respectively. The *no–slip boundary condition* (5) expresses that the flow and rigid body motion velocities coincide on the boundary of each rigid body B_j.

The motion of the rigid bodies is modeled by the following *Newton–Euler* equations

$$M_j \frac{d\mathbf{V}_j}{dt} = M_j \mathbf{g} + \mathbf{F}_j + \mathbf{F}_j^r, \quad j = 1, ..., J, \tag{6}$$

$$\frac{d(\mathbf{I}_j \boldsymbol{\omega}_j)}{dt} = \mathbf{T}_j + \overrightarrow{\mathbf{G}_j(t)\mathbf{x}_j} \times \mathbf{F}_j^r, \quad j = 1, ..., J, \tag{7}$$

where

$$\frac{d\mathbf{G}_j}{dt} = \mathbf{V}_j, \quad j = 1, ..., J. \tag{8}$$

In (6)–(7) M_j and $\mathbf{I}_j$ denote the *mass* and the *inertia tensor* of the j^{th} rigid body, respectively; $\mathbf{F}_j$ and $\mathbf{T}_j$ represent the resultant and the torque of the *hydrodynamical forces* acting on the j^{th} body, respectively, i.e.,

$$\mathbf{F}_j = -\int_{\gamma_j} \boldsymbol{\sigma}\mathbf{n} \, d\gamma_j, \quad \text{and} \quad \mathbf{T}_j = -\int_{\gamma_j} \overrightarrow{\mathbf{G}_j\mathbf{x}} \times \boldsymbol{\sigma}\mathbf{n} \, d\gamma_j,$$

with $\gamma_j = \partial B_j$. Finally $\mathbf{F}_j^r$ is a *short range repulsive force* acting on B_j introduced to prevent those particle/particle and particle/wall penetrations which may happen during the numerical simulation (see [30]). There is then a resulting torque in (7) acting on the point $\mathbf{x}_j$ where $\mathbf{F}_j^r$ applies on B_j. Equations (6)–(8) are completed by the following *initial conditions*:

$$B_j(0) = B_{0j}, \ \mathbf{G}_j(0) = \mathbf{G}_{0j}, \ \mathbf{V}_j(0) = \mathbf{V}_{0j}, \ \boldsymbol{\omega}_j(0) = \boldsymbol{\omega}_{0j}, \quad j = 1, ..., J. \tag{9}$$

To obtain a *variational formulation* of the problem (1)–(9), we introduce the following *space of compatible test functions*:

$$\begin{aligned} W_0(t) = \{ \, (\mathbf{v}, \mathbf{Y}, \boldsymbol{\theta}) \, | \, & \mathbf{v} \in (H^1(\Omega_f(t)))^d, \ \mathbf{v} = \mathbf{0} \text{ on } \Gamma, \ \mathbf{Y} = \{\mathbf{Y}_j\}_{j=1}^J \\ & \boldsymbol{\theta} = \{\boldsymbol{\theta}_j\}_{j=1}^J, \text{ with } \mathbf{Y}_j \in \mathbb{R}^d, \ \boldsymbol{\theta}_j \in \mathbb{R}^3, \ \mathbf{v}(\mathbf{x},t) = \mathbf{Y}_j + \boldsymbol{\theta}_j \times \overrightarrow{\mathbf{G}_j(t)\mathbf{x}}, \\ & \forall \, \mathbf{x} \in \partial B_j(t), \, \forall \, j = 1, ..., J \, \}. \end{aligned}$$

In the previous space we have $\boldsymbol{\theta}_j = (0, 0, \theta_j)$ if $d = 2$.

Applying the *virtual power principle* to the whole mixture (the fluid and

rigid bodies), yields the *global variational formulation*:

$$\rho_f \int_{\Omega_f(t)} \left[\frac{\partial \mathbf{u}}{\partial t} + (\mathbf{u}\cdot\boldsymbol{\nabla})\mathbf{u}\right]\cdot\mathbf{v}\,d\mathbf{x} + 2\mu\int_{\Omega_f(t)} \mathbf{D}(\mathbf{u}):\mathbf{D}(\mathbf{v})\,d\mathbf{x} - \int_{\Omega_f(t)} p\boldsymbol{\nabla}\cdot\mathbf{v}\,d\mathbf{x} + \sum_{j=1}^{J} M_j \frac{d\mathbf{V}_j}{dt}\cdot\mathbf{Y}_j + \sum_{j=1}^{J}\frac{d(\mathbf{I}_j\boldsymbol{\omega}_j)}{dt}\cdot\boldsymbol{\theta}_j = \rho_f\int_{\Omega_f(t)}\mathbf{g}\cdot\mathbf{v}\,d\mathbf{x} + \sum_{j=1}^{J}(M_j\mathbf{g}+\mathbf{F}_j^r)\cdot\mathbf{Y}_j + \sum_{j=1}^{J}\overrightarrow{\mathbf{G}_j\mathbf{x}_j}\times\mathbf{F}_j^r\cdot\boldsymbol{\theta}_j,\ \forall(\mathbf{v},\mathbf{Y},\boldsymbol{\theta})\in W_0(t), \tag{10}$$

$$\int_{\Omega_f(t)} q\boldsymbol{\nabla}\cdot\mathbf{u}(t)\,d\mathbf{x} = 0,\quad \forall q\in L^2(\Omega_f(t)), \tag{11}$$

$$\mathbf{u}(t) = \mathbf{g}_0(t)\ \text{ on }\ \Gamma, \tag{12}$$

$$\mathbf{u}(\mathbf{x},t) = \mathbf{V}_j(t) + \boldsymbol{\omega}_j(t)\times\overrightarrow{\mathbf{G}_j(t)\mathbf{x}},\quad \forall\mathbf{x}\in\partial B_j(t),\quad \forall j=1,...,J, \tag{13}$$

$$\frac{d\mathbf{G}_j}{dt} = \mathbf{V}_j,\quad \forall j=1,...,J, \tag{14}$$

to be completed by the initial conditions

$$\mathbf{u}(\mathbf{x},0) = \mathbf{u}_0(\mathbf{x}),\quad \forall\mathbf{x}\in\Omega_f(0), \tag{15}$$

$$B_j(0) = B_{0j},\ \mathbf{G}_j(0) = \mathbf{G}_{0j},\ \mathbf{V}_j(0) = \mathbf{V}_{0j},\ \boldsymbol{\omega}_j(0) = \boldsymbol{\omega}_{0j},\quad \forall j=1,...,J. \tag{16}$$

In relations (10)–(16) we have denoted by $\phi(t)$ the function $\mathbf{x}\to\phi(\mathbf{x},t)$. Moreover, we have used the following notation:

$$\mathbf{D}(\mathbf{u}) = \frac{1}{2}\left[\boldsymbol{\nabla}\mathbf{u} + (\boldsymbol{\nabla}\mathbf{u})^t\right]$$

$$\mathbf{a}\cdot\mathbf{b} = \sum_{k=1}^{d} a_k b_k,\ \forall\mathbf{a} = \{a_k\}_{k=1}^d,\ \mathbf{b} = \{b_k\}_{k=1}^d,$$

$$\mathbf{A}:\mathbf{B} = \sum_{k=1}^{d}\sum_{l=1}^{d} a_{kl}b_{kl},\ \forall\mathbf{A} = (a_{kl})_{1\le k,l\le d},\ \mathbf{B} = (b_{kl})_{1\le k,l\le d}.$$

In the above variational formulation it is reasonable to assume that $\mathbf{u}(t)$ belongs to $(H^1(\Omega_f(t)))^d$, and $p(t)$ belongs to $L^2(\Omega_f(t))$. We also have $\boldsymbol{\omega}_j(t) = (0,0,\omega_j(t))$ if $d=2$.

Formulations such as the one above, or closely related ones, have been used by other authors (see [35], [36], [46] and [47]) to simulate particulate flow via *arbitrary Lagrange–Euler* (ALE) methods using moving meshes. In this article we consider an alternative based on *fictitious domain methods* (also called *domain embedding methods*) and described with many details in [21] and [30], for instance. The main advantage of the fictitious domain approach is the possibility to achieve the flow related computation on a *fixed space region*, allowing the use of a *fixed mesh for the entire simulation*, which in fact represent a significant simplification from the computational point of view.

Actually, numerical methods in which the computational domain is remeshed are significantly more expensive because the mesh has to be refined in the region between particles (when they are close to each other), besides the need of repeated remeshing and projection.

2.2 A distributed Lagrange multiplier based fictitious domain formulation

In general terms our goal is to find a methodology with the following properties:

(a) A fixed mesh can be used for flow computations.

(b) The rigid body positions are obtained from the solution of the Newton–Euler equations of motion.

(c) The time discretization is done by operator splitting methods in order to treat individually the various operators occurring in the mathematical modeling

To achieve such a goal, we proceed as follows:

(i) We fill the rigid bodies with the surrounding fluid.

(ii) We assume that the fluid inside the rigid body has a rigid body motion.

(iii) We use (i) and (ii) to modify the global variational formulation.

(iv) We force the rigid motion inside each moving body via a Lagrange multiplier defined (distributed) over the body.

(v) We combine (iii) and (iv) to derive a variational formulation involving Lagrange multipliers to force the rigid body motion inside the moving bodies.

To obtain the modified variational formulation below this time we introduce the following space of *compatible test functions*:

$$\begin{aligned}\tilde{W}_0(t) = \{\, (\mathbf{v}, \mathbf{Y}, \boldsymbol{\theta}) \,|\, \mathbf{v} \in (H^1(\Omega))^d,\ \mathbf{v} = \mathbf{0} \text{ on } \Gamma, \mathbf{Y} = \{\mathbf{Y}_j\}_{j=1}^J,\ \boldsymbol{\theta} = \{\boldsymbol{\theta}_j\}_{j=1}^J,\\ \text{with } \mathbf{Y}_j \in \mathbb{R}^d,\ \boldsymbol{\theta}_j \in \mathbb{R}^3, \mathbf{v}(\mathbf{x}, t) = \mathbf{Y}_j + \boldsymbol{\theta}_j \times \overrightarrow{\mathbf{G}_j(t)\mathbf{x}},\\ \forall\, \mathbf{x} \in B_j(t),\ \forall\, j = 1, ..., J. \,\}\end{aligned}$$

We suppose (for simplicity) that B_j is made of an *homogeneous material* of density ρ_j; then, taking into account the fact that any rigid body motion velocity field $\mathbf{v}$ verifies $\nabla \cdot \mathbf{v} = 0$ and $\mathbf{D}(\mathbf{v}) = \mathbf{0}$, steps (i) to (iii) yield the following variant of the variational formulation (10)–(16):

For $t > 0$, find $\mathbf{u}(t) \in (H^1(\Omega))^d$, with $\mathbf{u}(t) = \mathbf{g}_0(t)$ on Γ, $p(t) \in L^2(\Omega)$, $\mathbf{G}_j(t) \in \mathbb{R}^d$, $\mathbf{V}_j(t) \in \mathbb{R}^d$, $\boldsymbol{\omega}_j(t) \in \mathbb{R}^3$, such that

$$\begin{aligned}
&\rho_f \int_\Omega \left[\frac{\partial \mathbf{u}}{\partial t} + (\mathbf{u}\cdot\boldsymbol{\nabla})\mathbf{u}\right]\cdot \mathbf{v}\, d\mathbf{x} + 2\mu\int_\Omega \mathbf{D}(\mathbf{u}) : \mathbf{D}(\mathbf{v})\, d\mathbf{x} - \int_\Omega p\boldsymbol{\nabla}\cdot\mathbf{v}\, d\mathbf{x} + \\
&\quad \sum_{j=1}^{J}(1-\frac{\rho_f}{\rho_j})M_j\,\frac{d\mathbf{V}_j}{dt}\cdot\mathbf{Y}_j + \sum_{j=1}^{J}(1-\frac{\rho_f}{\rho_j})\frac{d(\mathbf{I}_j\boldsymbol{\omega}_j)}{dt}\cdot\boldsymbol{\theta}_j = \\
&\quad \rho_f\int_\Omega \mathbf{g}\cdot\mathbf{v}\, d\mathbf{x} + \sum_{j=1}^{J}\left[(1-\frac{\rho_f}{\rho_j})M_j\,\mathbf{g} + \mathbf{F}_j^r\right]\cdot\mathbf{Y}_j + \\
&\quad \sum_{j=1}^{J}\overrightarrow{\mathbf{G}_j\mathbf{x}_j}\times\mathbf{F}_j^r\cdot\boldsymbol{\theta}_j, \quad \forall\,(\mathbf{v},\mathbf{Y},\boldsymbol{\theta}) \in \tilde{W}_0(t),
\end{aligned} \tag{17}$$

$$\int_\Omega q\boldsymbol{\nabla}\cdot\mathbf{u}\, d\mathbf{x} = 0,\ \forall\, q \in L^2(\Omega), \tag{18}$$

$$\mathbf{u}(\mathbf{x},t) = \mathbf{V}_j(t) + \boldsymbol{\omega}_j(t)\times\overrightarrow{\mathbf{G}_j(t)\mathbf{x}},\ \forall\,\mathbf{x}\in B_j(t), \quad \forall\, j = 1,...,J, \tag{19}$$

$$\frac{d\mathbf{G}_j}{dt} = \mathbf{V}_j, \quad \forall\, j = 1,...,J, \tag{20}$$

$$B_j(0) = B_{0j},\ \mathbf{G}_j(0) = \mathbf{G}_{0j},\ \mathbf{V}_j(0) = \mathbf{V}_{0j},\ \boldsymbol{\omega}_j(0) = \boldsymbol{\omega}_{0j}, \quad \forall\ j = 1,...,J, \tag{21}$$

$$\mathbf{u}(\mathbf{x},0) = \mathbf{u}_0(\mathbf{x}), \forall\,\mathbf{x}\in\Omega_f(0),\ \text{and}\ \mathbf{u}(\mathbf{x},0) = \mathbf{V}_{0j} + \boldsymbol{\omega}_{0j}\times\overrightarrow{\mathbf{G}_{0j}\mathbf{x}}, \forall\,\mathbf{x}\in B_{0j}. \tag{22}$$

Observe that in this formulation $\mathbf{u}(t)$ as well as $p(t)$ are defined over the entire domain Ω which contain the mixture (solid–liquid).

The family of *Lagrange multipliers* $\{\boldsymbol{\lambda}_j\}_{j=1}^J$, with $\boldsymbol{\lambda}_j \in \Lambda_j(t) := (H^1(B_j(t)))^d$, $j = 1,...,J$, is employed to relax the *rigid body motion constraint* (19). The following scalar products can be used in the formulation:

$$\begin{aligned}
&< \boldsymbol{\mu}, \mathbf{v} >_j = \int_{B(t)} (\boldsymbol{\mu}\cdot\mathbf{v} + \delta_j^2\nabla\boldsymbol{\mu} : \nabla\mathbf{v})\, d\mathbf{x},\ \forall\ \boldsymbol{\mu}\ \text{and}\ \mathbf{v}\in\boldsymbol{\Lambda}_j(t),\\
&< \boldsymbol{\mu}, \mathbf{v} >_j = \int_{B(t)} (\boldsymbol{\mu}\cdot\mathbf{v} + \delta_j^2\mathbf{D}(\boldsymbol{\mu}) : \mathbf{D}(\mathbf{v}))\, d\mathbf{x},\ \forall\ \boldsymbol{\mu}\ \text{and}\ \mathbf{v}\in\boldsymbol{\Lambda}_j(t),
\end{aligned}$$

with δ_j a *characteristic length* (the diameter of B_j, for example). We obtain, thus the following *fictitious domain formulation with Lagrange multipliers*:

For $t > 0$, find $\mathbf{u}(t) \in (H^1(\Omega))^d$, with $\mathbf{u}(t) = \mathbf{g}_0(t)$ on Γ, $p(t) \in L^2(\Omega)$, $\mathbf{G}_j(t) \in \mathbb{R}^d$, $\mathbf{V}_j(t) \in \mathbb{R}^d$, $\boldsymbol{\omega}_j(t) \in \mathbb{R}^3$, $\boldsymbol{\lambda}_j(t) \in \Lambda_j(t)$, such that

$$\begin{aligned}
&\rho_f \int_\Omega \left[\frac{\partial \mathbf{u}}{\partial t} + (\mathbf{u}\cdot\boldsymbol{\nabla})\mathbf{u}\right]\cdot \mathbf{v}\, d\mathbf{x} + 2\mu\int_\Omega \mathbf{D}(\mathbf{u}) : \mathbf{D}(\mathbf{v})\, d\mathbf{x} - \int_\Omega p\boldsymbol{\nabla}\cdot\mathbf{v}\, d\mathbf{x} + \\
&\quad \sum_{j=1}^J (1-\frac{\rho_f}{\rho_j}) M_j \frac{d\mathbf{V}_j}{dt}\cdot\mathbf{Y}_j + \sum_{j=1}^J (1-\frac{\rho_f}{\rho_j})\frac{d(\mathbf{I}_j\boldsymbol{\omega}_j)}{dt}\cdot\boldsymbol{\theta}_j - \\
&\quad \sum_{j=1}^J <\boldsymbol{\lambda}_j,\ \mathbf{v} - \mathbf{Y}_j - \boldsymbol{\theta}_j\times\overrightarrow{\mathbf{G}_j\mathbf{x}}>_j = \rho_f\int_\Omega \mathbf{g}\cdot\mathbf{v}\, d\mathbf{x} + \\
&\quad \sum_{j=1}^J \left[(1-\frac{\rho_f}{\rho_j})M_j\,\mathbf{g} + \mathbf{F}_j^r\right]\cdot\mathbf{Y}_j + \sum_{j=1}^J \overrightarrow{\mathbf{G}_j\mathbf{x}_j}\times\mathbf{F}_j^r\cdot\boldsymbol{\theta}_j, \\
&\qquad \forall\,(\mathbf{v},\mathbf{Y}_j,\boldsymbol{\theta}_j)\in (H_0^1(\Omega))^d\times\mathbb{R}^d\times\mathbb{R}^3,
\end{aligned} \tag{23}$$

$$\int_\Omega q\boldsymbol{\nabla}\cdot\mathbf{u}\, d\mathbf{x} = 0,\ \forall\, q\in L^2(\Omega), \tag{24}$$

$$<\boldsymbol{\mu}_j, \mathbf{u}(t) - \mathbf{V}_j(t) - \boldsymbol{\omega}_j(t)\times\overrightarrow{\mathbf{G}_j(t)\mathbf{x}}>_j = 0,\ \forall\,\boldsymbol{\mu}_j\in\Lambda_j(t),\ \forall\, j = 1,...,J, \tag{25}$$

$$\frac{d\mathbf{G}_j}{dt} = \mathbf{V}_j,\quad \forall\, j = 1,...,J, \tag{26}$$

$$B_j(0) = B_{0j},\ \mathbf{G}_j(0) = \mathbf{G}_{0j},\ \mathbf{V}_j(0) = \mathbf{V}_{0j},\ \boldsymbol{\omega}_j(0) = \boldsymbol{\omega}_{0j},\ \forall\, j = 1,...,J, \tag{27}$$

$$\mathbf{u}(\mathbf{x},0) = \mathbf{u}_0(\mathbf{x}),\ \forall\,\mathbf{x}\in\Omega_f(0) \text{ and } \mathbf{u}(\mathbf{x},0) = \mathbf{V}_{0j} + \boldsymbol{\omega}_{0j}\times\overrightarrow{\mathbf{G}_{0j}\mathbf{x}}, \forall\,\mathbf{x}\in B_{0j}. \tag{28}$$

Remark 1 *In (23)–(28) only the center of mass, the translation velocity of the center of mass, and the angular velocity of the particles are considered. Knowing this quantities one is able to translate and rotate any particle in space by tracking two extra points* $\mathbf{x}_1$ *and* $\mathbf{x}_2$ *on it. Then these points verify the rigid motion equation*

$$\begin{aligned}
\frac{d\mathbf{x}_i}{dt} &= \mathbf{V}(t) + \boldsymbol{\omega}(t)\times\overrightarrow{\mathbf{G}(t)\mathbf{x}_i},\ i = 1,2,\\
\mathbf{x}_i(0) &= \mathbf{x}_{i,0},\ i = 1,2.
\end{aligned}$$

This approach is very convenient in tree–dimensional problems, especially when the rigid bodies are non–spherical (see [23]). For two–dimensional problems, however, to find the orientation of the particles, it is easier to solve the equations

$$\frac{d\boldsymbol{\phi}_j}{dt} = \boldsymbol{\omega}_j,\ \textit{with}\ \boldsymbol{\phi}(0)_j = \boldsymbol{\phi}_j^0,\ \forall\, j = 1,...,J, \tag{29}$$

where $\boldsymbol{\phi}_j(t) = (0,0,\phi_j(t))$ *is the rotation angle and* $\boldsymbol{\omega}_j(t) = (0,0,\omega_j(t))$ *is the angular velocity of the* j*th body.*

Remark 2 *The fictitious domain approach, described above, has some common features with the immersed boundary method of C. Peskin (see, e.g., [54] and [55], but significant differences in the sense that it takes systematically advantage of distributed vector–valued Lagrange multipliers to force the rigid body motion inside the particles. As with the methods in [54] and [55], our approach takes*

advantage of the fact that the flow can be computed on a grid which does not have to vary in time, a substantial simplification indeed.

Remark 3 *An approach with some similarities to ours has been developed by S. Schwarzer et al [33] in a finite difference framework. In the above reference, the interaction between the rigid body and the fluid is forced via a* penalty method*, instead of the multiplier technique used in the present article; also minor particle–particle penetration is allowed and no enforcement of the rigid body motion inside the region occupied by the particle is done.*

Remark 4 *Since, in (23),* $\mathbf{u}$ *is* divergence free *and satisfies Dirichlet boundary conditions on* Γ*, we have*

$$2\int_\Omega \mathbf{D}(\mathbf{u}) : \mathbf{D}(\mathbf{v})\, d\mathbf{x} = \int_\Omega \boldsymbol{\nabla}\mathbf{u} : \boldsymbol{\nabla}\mathbf{v}\, d\mathbf{x},\ \forall\, \mathbf{v} \in (H_0^1(\Omega))^d,$$

which also represents a significant simplification from a computational point of view*, which is another plus for the fictitious domain approach used here.*

Remark 5 *Using High Energy Physics terminology, the multipliers* $\boldsymbol{\lambda}_j$ *can be viewed as* gluons *whose role is to force the rigidity inside* B_j *by matching the velocity fields of two continua. More precisely, the multipliers* $\boldsymbol{\lambda}_j$ *are mathematical objects of the* mortar *type, very close to those used in* domain decomposition methods *to match local solutions at interfaces or on overlapping regions (see ref. [1]). Indeed, the* $\boldsymbol{\lambda}$*'s in the present article have genuine mortar properties since their role is to force a fluid to behave like a rigid solid inside the space region occupied by the moving bodies.*

2.3 Treatment of collisions

With the mathematical model that we have considered it is not known if collisions can take place in finite time (in fact several scientists strongly believe that lubrication forces prevent these collisions in the case of viscous fluids). However, collisions take place in Nature and also in actual numerical simulations if special precautions are not taken. In the particular case of rigid bodies moving in a viscous fluid, under the effect of gravity and hydrodynamical forces, we shall assume that the collisions taking place are *smooth* ones in the sense that if two rigid bodies collide the rigid body velocities coincide at the points of contact. Similarly, we assume that if a rigid body hits the boundary, the rigid body and boundary velocities coincide at the points of contact. ¿From the smooth nature of these collisions the only precaution to be taken will be to avoid the overlapping of the regions occupied by the rigid bodies. To achieve this goal, we have included in the right–hand sides of the *Newton–Euler equations* (6) and (7), modeling the rigid body motion, a *short range repulsive force.*

If B_1 and B_2 are two rigid bodies of general shape with the points $\mathbf{x}_1$ and $\mathbf{x}_2$ from B_1 and B_2, respectively, realizing the shortest distance d between B_1 and B_2 ($d = |\mathbf{x}_1 - \mathbf{x}_2|$), we shall require the repulsion force $\mathbf{F}^{\mathrm{r}}$ between B_1 and B_2 to satisfy the following properties:

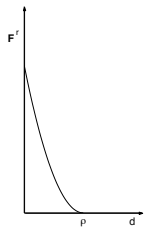

Figure 2: Repulsion force behavior

(i) To be parallel to $\overrightarrow{\mathbf{x}_1\mathbf{x}_2}$.

(ii) To verify

$$|\mathbf{F}^{\mathrm{r}}| = 0 \text{ if } d \geq \rho,$$
$$|\mathbf{F}^{\mathrm{r}}| = c/\epsilon \text{ if } d = 0,$$

(iii) $|\mathbf{F}^{\mathrm{r}}|$ has to behave as in Figure 2 for $0 \leq d \leq \rho$,

with c a scaling factor, ϵ a "small" positive number, and ρ the *range* of the repulsion force. For the simulations discussed in the following sections, we have taken $\rho \simeq h_\Omega$ (h_Ω is the *space discretization step* used for approximating the *velocity*). Body/wall collisions can be treated in a similar way. For a more detailed description of these repulsive forces see references [21] and [30].

2.4 Finite element approximation

For simplicity we assume that Ω is a polygonal domain in R^2. Let $h(= h_\Omega)$ be a *space discretization step*, $\mathcal{T}_h$ a finite element triangulation of $\overline{\Omega}$, and P_s the space of polynomials in two variables of degree $\leq s$. The two finite element approximations under considerations are the *Bercovier–Pironneau's* and the *Taylor–Hood's*. We describe first the approximation of the velocity and the pressure in problem (23)-(28) with these finite element methods:

(1) *Bercovier–Pironneau* (or **P1 iso P2/P1**). We construct another finite element triangulation $\mathcal{T}_{h/2}$ of $\overline{\Omega}$, which is twice finer than $\mathcal{T}_h$, by subdividing each triangle into 4 similar sub–triangles (8 sub–elements in 3D) by the midpoint sides (see Figure 3(a)). Then, we approximate respectively $(H^1(\Omega))^2$, and $L^2(\Omega)$ by the following finite dimensional spaces

$$W_h = \{\mathbf{v}_h \,|\, \mathbf{v}_h \in (C^0(\overline{\Omega}))^2,\ \mathbf{v}_h|_T \in P_1 \times P_1,\ \forall\, T \in \mathcal{T}_{h/2}\},$$
$$L^2_h = \{q_h \,|\, q_h \in C^0(\overline{\Omega}),\ q_h|_T \in P_1,\ \forall\, T \in \mathcal{T}_h\}.$$

(2) *Taylor–Hood* (or **P2/P1**). Unlike the previous element, here the approximations for velocity and pressure are defined on the same

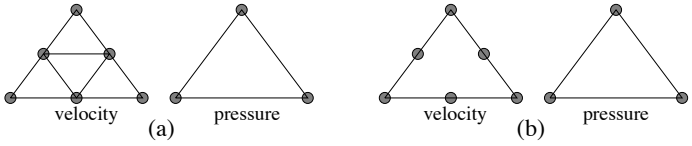

Figure 3: Degrees of freedom in the (a) *Bercovier–Pironneau*, and (b) *Taylor–Hood* elements.

triangulation $\mathcal{T}_h$ of $\overline{\Omega}$. The degrees of freedom for velocity and pressure are shown in Figure 3(b). The functional spaces $(H^1(\Omega))^2$ and $L^2(\Omega)$ are then approximated, respectively, by the following finite dimensional spaces

$$W_h = \{\mathbf{v}_h \,|\, \mathbf{v}_h \in (C^0(\overline{\Omega}))^2,\ \mathbf{v}_h|_T \in P_2 \times P_2,\ \forall T \in \mathcal{T}_h\},$$
$$L^2_h = \{q_h \,|\, q_h \in C^0(\overline{\Omega}),\ q_h|_T \in P_1,\ \forall T \in \mathcal{T}_h\}.$$

Concerning the spaces $(H^1_0(\Omega))^2$ and $L^2_0(\Omega) := \{q \in L^2(\Omega) \,|\, \int_\Omega q\, d\mathbf{x} = 0\}$, we respectively use the following finite dimensional approximations

$$W_{0h} = \{\mathbf{v}_h \,|\, \mathbf{v}_h \in W_h,\ \mathbf{v}_h = \mathbf{0}\ on\ \Gamma\},$$
$$L^2_{0h} = \{q_h \,|\, q_h \in L^2_h, \int_\Omega q_h\, d\mathbf{x} = 0\},$$

where W_h and L^2_h are the corresponding finite dimensional spaces obtained by the *Bercovier–Pironneau* or the *Taylor–Hood* finite element approximations. Now, to find a finite element approximation of the Lagrange multipliers $\lambda_j(t)$, for $j = 1, ..., J$, we construct a finite element triangulation $\mathcal{T}^j_h(t)$ of $\overline{B_j(t)}$ (see Figure 4 (a)). Let $\mathcal{T}^j_{h/2}(t)$ another finite element triangulation twice finer. The functional spaces $\Lambda_j(t) = (H^1(B_j(t)))^d$, are then approximated by

$$\Lambda_{jh}(t) = \{\boldsymbol{\mu}_h | \boldsymbol{\mu}_h \in (C^0(\overline{B_{jh}(t)}))^2,\ \boldsymbol{\mu}_h|_T \in P_1 \times P_1,\ \forall T \in \mathcal{T}^j_{h/2}(t)\},$$

when using the Bercovier–Pironneau element, and

$$\Lambda_{jh}(t) = \{\boldsymbol{\mu}_h | \boldsymbol{\mu}_h \in (C^0(\overline{B_{jh}(t)}))^2,\ \boldsymbol{\mu}_h|_T \in P_2 \times P_2,\ \forall T \in {\mathcal{T}_h}^j(t)\},$$

when using the Taylor–Hood element. An alternative to approximate the Lagrange multipliers $\lambda_j(t)$ is as follows: Let $\{\mathbf{x}_i\}_{i=1}^{N_j}$ be a set of points from $\overline{B_j(t)}$ which cover $\overline{B_j(t)}$. We define

$$\Lambda_{jh}(t) = \{\boldsymbol{\mu}_h | \boldsymbol{\mu}_h = \sum\nolimits_{i=1}^{N_j} \boldsymbol{\mu}_i \delta(\mathbf{x} - \mathbf{x}_i),\ \boldsymbol{\mu}_i \in \mathbb{R}^2,\ \forall i = 1, ..., N_j\}, \tag{30}$$

where $\delta(\cdot)$ is the Dirac measure at $\mathbf{x} = \mathbf{0}$. Then, instead of the scalar product (3.6) we use $< \cdot, \cdot >_{jh}$ defined by

$$< \boldsymbol{\mu}_h, \mathbf{v}_h >_{jh} = \sum\nolimits_{i=1}^{N_j} \boldsymbol{\mu}_i \cdot \mathbf{v}_h(\mathbf{x}_i),\ \forall \boldsymbol{\mu}_h \in \Lambda_{jh}(t),\ \mathbf{v}_h \in W_h. \tag{31}$$

(a) (b)

Figure 4: (a) A finite element triangulation of $\overline{B_{jh}(t)}$. (b) Set of nodes inside $\overline{B_{jh}(t)}$ from the velocity grid and control points on $\partial B_j(t)$ to enforce rigid body motion by the *collocation method*.

The approach based on (30) and (31) makes little sense for the continuous problem, but is meaningful for the discrete problem; it amounts to forcing the rigid body motion of $B_j(t)$ via a *collocation method*. A similar technique has been used to enforce Dirichlet boundary conditions by F. Bertrand et al. (ref. [9]). Moreover, the set of points $\{\mathbf{x}_i\}_{i=1}^{N_j}$ can be chosen as the set of *nodes* of the velocity grid which are contained in $B_j(t)$, at a distance of $\partial B_j(t) \geq c\,h$ (with $c \approx 1$), plus a set of control points located on $\partial B_j(t)$ (see Figure 4(b) for the case in which the Taylor–Hood element is used). This *hybrid* approach is easier to implement and is particularly well suited when the boundary ∂B_j has corners or edges.

Using the above finite dimensional spaces leads to the following approximation of problem (23)–(28), (29):

For $t > 0$, find $\mathbf{u}_h(t) \in W_h$, with $\mathbf{u}_h(t) = \mathbf{g}_{0h}(t)$ on Γ, $p_h(t) \in L^2_{0h}(\Omega)$, $\mathbf{G}_j(t) \in \mathbb{R}^d$, $\mathbf{V}_j(t) \in \mathbb{R}^d$, $\boldsymbol{\phi}_j(t) \in \mathbb{R}^3$, $\boldsymbol{\omega}_j(t) \in \mathbb{R}^3$, $\boldsymbol{\lambda}_{jh}(t) \in \Lambda_{jh}(t)$, such that

$$
\begin{aligned}
&\rho_f \int_\Omega \left[\frac{\partial \mathbf{u}_h}{\partial t} + (\mathbf{u}_h \cdot \boldsymbol{\nabla})\mathbf{u}_h\right] \cdot \mathbf{v}\, d\mathbf{x} + \mu \int_\Omega \boldsymbol{\nabla}\mathbf{u}_h : \boldsymbol{\nabla}\mathbf{v}\, d\mathbf{x} - \int_\Omega p_h \boldsymbol{\nabla}\cdot \mathbf{v}\, d\mathbf{x} + \\
&\quad \sum_{j=1}^J (1 - \frac{\rho_f}{\rho_j}) M_j \frac{d\mathbf{V}_j}{dt} \cdot \mathbf{Y}_j \; + \sum_{j=1}^J (1 - \frac{\rho_f}{\rho_j}) \frac{d(\mathbf{I}_j \boldsymbol{\omega}_j)}{dt} \cdot \boldsymbol{\theta}_j \; - \\
&\quad \sum_{j=1}^J < \boldsymbol{\lambda}_{jh},\; \mathbf{v} - \mathbf{Y}_j - \boldsymbol{\theta}_j \times \overrightarrow{\mathbf{G}_j \mathbf{x}} >_{jh} = \rho_f \int_\Omega \mathbf{g} \cdot \mathbf{v}\, d\mathbf{x} + \\
&\quad \sum_{j=1}^J \left[(1 - \frac{\rho_f}{\rho_j}) M_j\, \mathbf{g} + \mathbf{F}_j^r\right] \cdot \mathbf{Y}_j + \sum_{j=1}^J \overrightarrow{\mathbf{G}_j \mathbf{x}_j} \times \mathbf{F}_j^r \cdot \boldsymbol{\theta}_j, \\
&\qquad \forall\, (\mathbf{v}, \mathbf{Y}_j, \boldsymbol{\theta}_j) \in W_{0h} \times \mathbb{R}^d \times \mathbb{R}^3,
\end{aligned}
\tag{32}
$$

$$\int_\Omega q\boldsymbol{\nabla}\cdot\mathbf{u}_h\,d\mathbf{x}=0,\ \forall\, q\in L^2_h(\Omega), \tag{33}$$

$$<\boldsymbol{\mu}_j,\mathbf{u}_h(t)-\mathbf{V}_j(t)-\boldsymbol{\omega}_j(t)\times\overrightarrow{\mathbf{G}_j(t)\mathbf{x}}>_{jh}=0,\ \forall\,\boldsymbol{\mu}_j\in\Lambda_{jh}(t),\ \forall\, j=1,...,J, \tag{34}$$

$$\frac{d\mathbf{G}_j}{dt}=\mathbf{V}_j,\quad \frac{d\boldsymbol{\phi}_j}{dt}=\boldsymbol{\omega}_j\quad\forall\, j=1,...,J, \tag{35}$$

$$B_j(0)=B_{0j},\ \mathbf{G}_j(0)=\mathbf{G}_{0j},\ \mathbf{V}_j(0)=\mathbf{V}_{0j},\ \boldsymbol{\phi}_j(0)=\boldsymbol{\phi}_{0j},\ \boldsymbol{\omega}_j(0)=\boldsymbol{\omega}_{0j},\quad \forall\, j=1,...,J, \tag{36}$$

$$\mathbf{u}_h(\mathbf{x},0)=\mathbf{u}_{0h}(\mathbf{x}),\forall\,\mathbf{x}\in\Omega_f(0)\text{ and }\mathbf{u}_h(\mathbf{x},0)=\mathbf{V}_{0j}+\boldsymbol{\omega}_{0j}\times\overrightarrow{\mathbf{G}_{0j}\mathbf{x}},\forall\,\mathbf{x}\in B_{0j}. \tag{37}$$

In the previous formulation, $\mathbf{g}_{0h}$ is an approximation on Γ of the boundary function $\mathbf{g}_0$, belonging to the trace of W_h on Γ. This approximation must verify $\int_\Gamma \mathbf{g}_{0h}\cdot\mathbf{n}\,d\Gamma=0$.

2.5 Time discretization by operator splitting

Following A. Chorin (refs. [11]–[13]), most "modern" Navier–Stokes solvers are based on *operator splitting* schemes (see, e.g., refs. [31], [70]) in order to force the incompressibility condition via a Stokes solver or a L^2–projection method. This approach still applies to the initial value problem (32)–(37) which contains five numerical difficulties to each of which can be associated a specific operator, namely

(a) The incompressibility condition and the related unknown pressure.

(b) An advection term.

(c) A diffusion term.

(d) The rigid body motion of $B_j(t)$ and the related multiplier $\boldsymbol{\lambda}_j(t)$.

(e) The collision terms $\mathbf{F}^r_j$.

The operators in (a) and (d) are essentially *projection operators*. ¿From an abstract point of view, problem (32)–(37) is a particular case of the following class of initial value problems

$$\frac{d\psi}{dt}+\sum_{i=1}^{5}A_i(\psi,t)=f,\ \psi(0)=\psi_0, \tag{38}$$

where the operators $A_{\rm i}$ can be *multivalued*. Among the many operator–splitting methods which can be employed to solve problem (38) we advocate (following, e.g., [48]) the very simple one below; it is only *first order accurate* but its low order accuracy is compensated by good stability and robustness properties. Actually, this scheme can be made *second order accurate by symmetrization* (see, e.g., [7], [17] for the application of *symmetrized splitting schemes* to the solution of the Navier–Stokes equations).

A fractional step scheme à la Marchuk–Yanenko: Let $\triangle t(>0)$ be a *time discretization step*, given $\psi^0=\psi_0$, compute ψ^{n+1} from ψ^n via

$$\frac{\psi^{n+i/5}-\psi^{n+(i-1)/5}}{\triangle t}+A_i(\psi^{n+i/5},t^{n+1})=f_i^{n+1}, \tag{39}$$

for $i=1,2,3,4,5$ with $t^n=n\triangle t$ and $\sum_{i=1}^5 f_i^{n+1}=f^{n+1}$.

Applying scheme (39) to the problem (32)–(37), we obtain the following scheme (after dropping some of the subscripts h): Given $\mathbf{u}^0=\mathbf{u}_{0h}$, $\mathbf{V}_j^0$, ω_j^0, B_j^0, $\mathbf{G}_j^0$, and assuming we know $\mathbf{u}^n$, $\mathbf{V}_j^n$, ω_j^n, B_j^n, $\mathbf{G}_j^n$, for $n\geq 0$,

Step 1. Find $\mathbf{u}^{n+1/5}\in W_h$ with $\mathbf{u}^{n+1/5}=\mathbf{g}_{0h}^{n+1}$ on Γ, and $p^{n+1/5}\in L^2_{0h}$ such that

$$\begin{aligned}&\rho_f\int_\Omega\frac{\mathbf{u}^{n+1/5}-\mathbf{u}^n}{\Delta t}\cdot\mathbf{v}\,d\mathbf{x}\ -\int_\Omega p^{n+1/5}\boldsymbol{\nabla}\cdot\mathbf{v}d\mathbf{x}=0,\ \forall\,\mathbf{v}\in W_{0h},\\&\int_\Omega q\boldsymbol{\nabla}\cdot\mathbf{u}^{n+1/5}d\mathbf{x}=0,\ \forall\,q\in L^2_h,\end{aligned} \tag{40}$$

Step 2. Next, find $\mathbf{u}^{n+2/5}=\mathbf{u}(t^{n+1})$, where $\mathbf{u}(t)$ is the solution on (t^n,t^{n+1}) of the following advection problem

$$\begin{aligned}&\int_\Omega\frac{\partial\mathbf{u}(t)}{\partial t}\cdot\mathbf{v}\,d\mathbf{x}+\int_\Omega(\mathbf{u}^{n+1/5}\cdot\boldsymbol{\nabla})\mathbf{u}(t)\cdot\mathbf{v}\,d\mathbf{x}=0\ \ \forall\,\mathbf{v}\in W_{0h}^{n+1,-},\\&\mathbf{u}(t^n)=\mathbf{u}^{n+1/5},\ \text{and}\ \mathbf{u}(t)=\mathbf{g}_{0h}(t^{n+1})\ \text{on}\ \Gamma_-^{n+1}\times(t^n,t^{n+1}),\end{aligned} \tag{41}$$

with $\Gamma_-^{n+1}=\{\mathbf{x}\,|\,\mathbf{x}\in\Gamma,\,\mathbf{g}_{0h}^{n+1}\cdot\mathbf{n}(\mathbf{x})<0\}$ and
$W_{0h}^{n+1,-}=\{\mathbf{v}\,|\,\mathbf{v}\in W_h,\,\mathbf{v}=0\ \text{on}\ \Gamma_-^{n+1}\}$.

Step 3. Find $\mathbf{u}^{n+3/5}\in W_h$ with $\mathbf{u}^{n+3/5}=\mathbf{g}_{0h}^{n+1}$ on Γ such that

$$\int_\Omega\frac{\mathbf{u}^{n+3/5}-\mathbf{u}^{n+2/5}}{\triangle t}\cdot\mathbf{v}\,d\mathbf{x}+\mu\int_\Omega\boldsymbol{\nabla}\mathbf{u}^{n+3/5}:\boldsymbol{\nabla}\mathbf{v}\,d\mathbf{x}=\int_\Omega\mathbf{g}\cdot\mathbf{v}d\mathbf{x},\ \forall\,\mathbf{v}\in W_{0h}. \tag{42}$$

Step 4. Predict the motion of the center of mass and the angular velocity of the rigid bodies via the solution on (t^n,t^{n+1}) of

$$\begin{aligned}&(1-\frac{\rho_f}{\rho_j})M_j\frac{d\mathbf{V}_j}{dt}=(1-\frac{\rho_f}{\rho_j})M_j\mathbf{g}+\mathbf{F}_j^r,\\&(1-\frac{\rho_f}{\rho_j})\frac{d(\mathbf{I}_j\,\boldsymbol{\omega}_j)}{dt}=\overrightarrow{\mathbf{G}_jx_j}\times\mathbf{F}_j^r,\\&\frac{d\mathbf{G}_j}{dt}=\mathbf{V}_j(t),\\&\frac{d\boldsymbol{\phi}_j}{dt}=\boldsymbol{\omega}_j(t),\\&\mathbf{V}_j(t^n)=\mathbf{V}_j^n,\ \boldsymbol{\omega}_j(t^n)=\boldsymbol{\omega}_j^n,\ \mathbf{G}_j(t^n)=\mathbf{G}_j^n,\end{aligned} \tag{43}$$

for $j = 1, ..., J$, and set $\mathbf{V}_j^{n+4/5} = \mathbf{V}_j(t^{n+1})$, $\boldsymbol{\omega}_j^{n+4/5} = \boldsymbol{\omega}_j(t^{n+1})$, $\mathbf{G}_j^{n+4/5} = \mathbf{G}_j(t^{n+1})$, $\mathbf{u}^{n+4/5} = \mathbf{u}^{n+3/5}$.

Step 5. With the center $\mathbf{G}_j^{n+4/5}$ obtained at the above step, we enforce the rigid body motion in the region $B_j(t^{n+4/5})$ occupied by the rigid body. So we look for $\mathbf{u}^{n+1} \in W_h^{n+1}$, $\mathbf{V}_j^{n+1} \in \mathbb{R}^3$, $\boldsymbol{\omega}_j^{n+1} \in \mathbb{R}^3$, and $\boldsymbol{\lambda}_j^{n+4/5} \in \Lambda_{jh}^{n+4/5}$, such that

$$
\begin{aligned}
&\rho_f \int_\Omega \frac{\mathbf{u}^{n+1} - \mathbf{u}^{n+4/5}}{\triangle t} \cdot \mathbf{v}\, d\mathbf{x} + \sum_{j=1}^{J} (1 - \frac{\rho_f}{\rho_j}) M_j \frac{{\mathbf{V}_j}^{n+1} - \mathbf{V}_j^{n+4/5}}{\triangle t} \cdot \mathbf{Y}_j \; + \\
&\quad \sum_{j=1}^{J} (1 - \frac{\rho_f}{\rho_j}) \frac{(\mathbf{I}_j\, \boldsymbol{\omega}_j)^{n+1} - (\mathbf{I}_j\, \boldsymbol{\omega}_j)^{n+4/5}}{\triangle t} \cdot \boldsymbol{\theta}_j \; = \\
&\quad \sum_{j=1}^{J} < \boldsymbol{\lambda}_j^{n+4/5}, \mathbf{v} - \mathbf{Y}_j - \boldsymbol{\theta}_j \times \overrightarrow{\mathbf{G}_j^{n+4/5}\mathbf{x}} >_{jh}, \\
&\qquad \forall \mathbf{v} \in V_{0h}, \mathbf{Y}_j \in \mathbb{R}^d,\ \boldsymbol{\theta}_j \in \mathbb{R}^3, \\
&< \boldsymbol{\mu}_j, \mathbf{u}^{n+1} - \mathbf{V}_j^{n+1} - \boldsymbol{\omega}_j^{n+1} \times \overrightarrow{\mathbf{G}_j^{n+4/5}\mathbf{x}} >_{jh} = 0,\ \forall\, \boldsymbol{\mu}_j \in \Lambda_{jh}^{n+4/5}.
\end{aligned}
\tag{44}
$$

Problems (40) and (44) are finite dimensional linear problems with the structure

$$
\begin{cases}
\mathbf{A}\mathbf{x} + \mathbf{B}^t\mathbf{y} = \mathbf{b}, \\
\mathbf{B}\mathbf{x} = \mathbf{c},
\end{cases}
\tag{45}
$$

where matrix $\mathbf{A}$ is *symmetric*; actually matrix $\mathbf{A}$ associated to problem (40) is *positive definite*, while matrix $\mathbf{A}$ associated to problem (44) is *positive definite* if $\rho_j > \rho_f$, $\forall\, j = 1, ..., J$. Problems such as (45) are known as *Kuhn–Tucker* or (*saddle–point*) *systems* and their *iterative solution* by *Uzawa/conjugate gradient algorithms* is discussed with many details in, e.g., [20] and [24]. The solution of problems (40) and (44) by the algorithms in [20] and [24] is discussed, again with many details, in [25], [27], [28], and [29].

Problem (42) is a *discrete elliptic system* whose iterative or direct solution is a quite classical problem. On the other hand, solving the *pure advection problem* (41) is a more delicate issue. Problem (41) can be solved by a *method of characteristics* as in [31] and [56]. An easy–to–implement alternative is provided by the *wave–like equation* method discussed in [17] and [18]. Problem (43) is solved by a subcycling and predicting–correcting technique with local time time step $\Delta t/N$ as in [30]. In fact, one of the main advantages of the operator–splitting methodology is that it allows the use of time steps much smaller than Δt to predict and correct the position velocity and of the centers of mass, as well as the angular velocity and orientation of the rigid bodies. For our calculations we have taken $N = 10$ or 20. Observe that, between collisions $\mathbf{F}_j^r = \mathbf{0}$, and it is possible to obtain an exact solution of system (43).

3 Fluid flow with free boundaries

In this section we discuss a methodology for the numerical solution of a time–dependent two–dimensional viscous free–surface flow with applications to lubrication and coating technology. This methodology combines finite element approximation, time discretization by operator–splitting, and a Taylor–Galerkin scheme for the relocation of the free boundary. A nice feature of this approach is that it avoids iterative procedures to update the position of the free boundary, and that a stable isoparametric finite element approximation of low order is used to handle the geometry of the curved domain. The structure of the discrete equations is the same as in the fixed boundary case, so that we can extend existing Navier–Stokes solvers to the solution of these new problems. The above methodology is applied to the solution of two–dimensional viscous free–surface flow, with potential applications to coating flow.

Many flow problems in physics and applied sciences lead to the incompressible Navier–Stokes equations with a free capillary surface. These flows have many important industrial applications. From the great variety of possible applications we mention the so called "coating flows" [45], [58], and flow in semiconductor melts [5], [67]. On a capillary free surface the normal stress of the flow field is balanced by surface tension. These flows are modeled under the assumption that the surface tension is proportional to the curvature of the free surface, therefore surface tension plays a significant role in determining the shape of the free surface. This model has been studied extensively experimentally [59], theoretically [3], [6], [50], [61], [68], asymptotically [44], and numerically [4], [15], [43], [62], [66]. In particular, an interesting discussion of a flow down an inclined perturbed plane can be found in [60]; it includes a detailed comparison between experimental measurements, lubrication approximations, and numerical results.

The numerical methods most widely used today rely on space approximation by Galerkin/finite element methods for the following reasons: formulated in this way, the free surface problem takes an elegant and concise form with the boundary condition incorporated within the equations in a straightforward manner; these methods are particularly well–suited to coping with the highly deformed free boundaries and irregular flow domains that arise in these problems. Discretizing these kind of problems causes additional numerical difficulties due to the free boundary curvature related terms, and the fact that the solution domain is not known in advance. It is well known that the most crucial issue in these problems is the treatment of the curvature terms. Thus, many authors prefer to treat these terms in an implicit way, and generally a kind of iterative procedure is applied to locate the free surface. In addition, isoparametric quadratic finite element approximations are very common along with a quadratic or cubic parametrization of the free surface which leads to additional complications. Analysis of the convergence properties and/or stability of some computational techniques can be found in e.g. [4], [49], and [65].

The numerical solution of free boundary problems is still an active field

of research and new efficient computational methods are needed to solve this kind of problems. In this work we consider the numerical solution of a time–dependent two–dimensional viscous free–surface flow with applications to lubrication and coating technology; its formulation is given in Section 3.1. We take advantage of operator splitting methods, as shown in Section 3.2, to avoid iterative procedures for locating the free boundary; generally these procedures are quite costly for practical calculations. In addition, the global variational formulation is modified to decouple the two velocity components from the deformation tensor, resulting in a significant simplification from the computational point of view. Then, in Section 3.3, we introduce an isoparametric version of the Bercovier–Pironneau finite element method ([10], [21]) to achieve the space discretization. The resulting discrete equations have the same structure as in usual problems modeled by the Navier–Stokes equations, with, however, an additional equation taking care of the relocation of the free surface.

3.1 Formulation of the problem

Let $\Omega(t)$ be a two–dimensional space region, periodic in the horizontal direction, which contains an incompressible viscous fluid of density ρ, with a free capillary surface $\gamma(t)$ as shown in Figure 5. We shall assume that the free boundary $\gamma(t)$ can be described by a time dependent function $\eta(x_1, t)$, $x_1 \in [0, L]$, $t \geq 0$. Assuming that the only external force acting on the fluid is gravity, denoted by $\mathbf{g}$, the fluid flow is modeled by the Navier–Stokes equations completed by appropriate initial and boundary conditions:

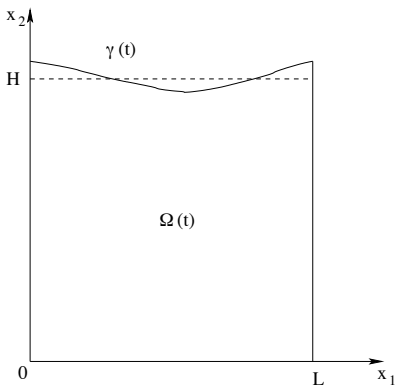

Figure 5: Flow region with a free boundary

$$\rho\left[\frac{\partial \mathbf{u}}{\partial t}+(\mathbf{u}\cdot\boldsymbol{\nabla}\mathbf{u})\right]=\rho\,\mathbf{g}+\boldsymbol{\nabla}\cdot\boldsymbol{\sigma}\quad\text{in }\Omega(t),\ 0<t\le T, \tag{46}$$

$$\boldsymbol{\nabla}\cdot\mathbf{u}=0\quad\text{in }\Omega(t),\ 0<t\le T, \tag{47}$$

$$\mathbf{u}(\mathbf{x},0)=\mathbf{u}_0(\mathbf{x}),\quad\forall\mathbf{x}\in\Omega(0), \tag{48}$$

$$\mathbf{u}(x_1,0,t)=\mathbf{0},\quad\forall\,t\in(0,T),\ x_1\in(0,L), \tag{49}$$

$$\mathbf{u}(0,x_2,t)=\mathbf{u}(L,x_2,t),\ \forall\,t\in(0,T),\ x_2\in(0,\eta(0,T)), \tag{50}$$

$$\boldsymbol{\sigma}\mathbf{n}=s\,\mathcal{H}(\eta)\,\mathbf{n}\quad\text{on }\gamma(t),\ \text{with } s\in R, \tag{51}$$

$$\frac{\partial\eta}{\partial t}\,n_2=\mathbf{u}\cdot\mathbf{n}\quad\text{on }\gamma(t),\ \text{with }\eta(0,t)=\eta(L,t),\quad 0<t\le T, \tag{52}$$

where $\mathbf{u}$ denotes the velocity of the fluid, $\boldsymbol{\sigma}=\mu\,[\boldsymbol{\nabla}\mathbf{u}+(\boldsymbol{\nabla}\mathbf{u})^t]-p\,\mathbf{I}$ is the *stress–tensor* for a *Newtonian fluid* of viscosity μ and pressure p; we denote by $\mathbf{n}=(n_1,n_2)$ the unit normal vector on the boundary of $\Omega(t)$ and pointing outward to the flow region. The initial velocity $\mathbf{u}_0(\mathbf{x})$ is periodic at $x_1=0$ and $x_1=L$ and satisfies $\boldsymbol{\nabla}\cdot\mathbf{u}_0=0$. Also, in (50) we assume $\eta(0,T)=\eta(L,T)$. In the above model, s is the coefficient of surface tension, and $\mathcal{H}(\eta)$ is the curvature of the free boundary, defined by

$$\mathcal{H}(\eta)=\frac{\partial^2\eta}{\partial x_1^2}\Big/\left(1+\left|\frac{\partial\eta}{\partial x_1}\right|^2\right)^{3/2}. \tag{53}$$

3.2 Time discretization by operator splitting

Suppose that at an arbitrary time t we know the flow region $\Omega(t)$. We introduce the following test function space:

$$\begin{aligned}\mathbf{V}_0(t)=\{\mathbf{v}\,|\,\mathbf{v}\in(H^1(\Omega(t)))^2,\ \mathbf{v}=\mathbf{0}\ \text{if } x_2=0,\mathbf{v}\ \text{periodic at}\\ x_1=0\ \text{and}\ x_1=L\}.\end{aligned} \tag{54}$$

The variational formulation of equations (46)–(51) is:

$$\begin{aligned}&\rho\int_{\Omega(t)}\left[\frac{\partial\mathbf{u}}{\partial t}+(\mathbf{u}\cdot\boldsymbol{\nabla}\mathbf{u})\right]\cdot\mathbf{v}\,d\mathbf{x}+2\mu\int_{\Omega(t)}\mathbf{D}(\mathbf{u}):\mathbf{D}(\mathbf{v})\,d\mathbf{x}-\int_{\Omega(t)}p\boldsymbol{\nabla}\cdot\mathbf{v}\,d\mathbf{x}=\\ &\qquad\rho\int_{\Omega(t)}\mathbf{g}\cdot\mathbf{v}\,d\mathbf{x}+s\int_{\gamma(t)}\mathcal{H}(\eta(t))\,\mathbf{n}\cdot\mathbf{v}\,d\gamma(t),\ \forall\,\mathbf{v}\in\mathbf{V}_0(t),\end{aligned} \tag{55}$$

$$\int_{\Omega(t)}q\,\boldsymbol{\nabla}\cdot\mathbf{u}\,d\mathbf{x}=0,\quad\forall\,q\in L^2(\Omega(t)), \tag{56}$$

$$\frac{\partial\eta}{\partial t}+u_1\frac{\partial\eta}{\partial x_1}=u_2,\quad\text{on }\gamma(t),\ \text{with }\eta(0,t)=\eta(L,t),\quad 0<t\le T, \tag{57}$$

where $\mathbf{D}(\mathbf{u})=\frac{1}{2}\,[\boldsymbol{\nabla}\mathbf{u}+(\boldsymbol{\nabla}\mathbf{u})^t]$ is the deformation tensor, see [22] for more details.

Operator–splitting methods apply to this problem which contain three numerical difficulties, namely: (a) the incompressibility condition and the related unknown pressure, (b) an advection term, and (c) the relocation of the

free boundary. We apply again a fractional step scheme à la Marchuk–Yanenko ([48]). First, we define the following space of test functions which is used in the scheme below:

$$\mathbf{W}_-^{n+1/4} = \{\mathbf{v} \mid \mathbf{v} \in (H^1(\Omega^n))^2, \mathbf{v} = \mathbf{0} \text{ on } \Gamma_-^{n+1/4},\ \mathbf{v} \text{ periodic at } x_1 = 0 \text{ and } x_1 = L\}, \tag{58}$$

with

$$\Gamma_-^{n+1/4} = \{\mathbf{x} \mid \mathbf{x} \in \gamma^n,\ \mathbf{u}^{n+1/4} \cdot \mathbf{n}(\mathbf{x}) < 0\}. \tag{59}$$

Then, the scheme after operator–splitting reads as follows: Let $\triangle t$ be a time discretization step, and $\Omega^n = \Omega(n\triangle t)$, $\eta^n = \eta(n\triangle t)$, $\mathbf{u}^n = \mathbf{u}(n\triangle t)$, $\gamma^n = \gamma(n\triangle t)$, $\mathbf{V}_0^n = \mathbf{V}_0(n\triangle t)$. For $n \geq 0$, $\mathbf{u}^n$, η^n, Ω^n, γ^n being known, solve the following problems:

Find $\mathbf{u}^{n+1/4} \in \mathbf{V}_0^n$ and $p^{n+1/4} \in L^2(\Omega^n)$ such that

$$\begin{aligned}
&\rho \int_{\Omega^n} \frac{\mathbf{u}^{n+1/4} - \mathbf{u}^n}{\triangle t} \cdot \mathbf{v}\, d\mathbf{x} + \frac{\mu}{2} \int_{\Omega^n} \boldsymbol{\nabla} \mathbf{u}^{n+1/4} : \boldsymbol{\nabla} \mathbf{v}\, d\mathbf{x} - \int_{\Omega^n} p^{n+1/4} \boldsymbol{\nabla} \cdot \mathbf{v}\, d\mathbf{x} \ = \\
&\quad s \int_{\gamma^n} \mathcal{H}(\eta^n)\, \mathbf{n} \cdot \mathbf{v}\, d\gamma^n + \int_{\Omega^n} \mathbf{g} \cdot \mathbf{v}\, d\mathbf{x} - \frac{\mu}{2} \int_{\Omega^n} (\boldsymbol{\nabla} \mathbf{u}^n)^t : \boldsymbol{\nabla} \mathbf{v}\, d\mathbf{x} \quad \forall\, \mathbf{v} \in \mathbf{V}_0^n, \\
&\int_{\Omega^n} q\, \boldsymbol{\nabla} \cdot \mathbf{u}^{n+1/4}\, d\mathbf{x} = 0, \quad \forall\, q \in L^2(\Omega^n).
\end{aligned} \tag{60}$$

Compute $\mathbf{u}^{n+2/4}$ via the solution of the following pure advection problem on $\Omega^n \times (t^n, t^{n+1})$

$$\begin{aligned}
&\int_{\Omega^n} \frac{\partial \mathbf{u}}{\partial t} \cdot \mathbf{v}\, d\mathbf{x} + \int_{\Omega^n} (\mathbf{u}^{n+1/4} \cdot \boldsymbol{\nabla}) \mathbf{u} \cdot \mathbf{v}\, d\mathbf{x} = 0,\ \forall\, \mathbf{v} \in \mathbf{W}_-^{n+1/4}, \\
&\mathbf{u}(t^n) = \mathbf{u}^{n+1/4}, \\
&\mathbf{u}(t) = \mathbf{u}^{n+1/4} \text{ on } \Gamma_-^{n+1/4} \times (t^n, t^{n+1}), \\
&\text{and set } \mathbf{u}^{n+2/4} = \mathbf{u}(t^{n+1}).
\end{aligned} \tag{61}$$

Next, find $\mathbf{u}^{n+3/4} \in \mathbf{V}_0^n$ and $p^{n+3/4} \in L^2(\Omega^n)$, by solving the problem

$$\begin{aligned}
&\rho \int_{\Omega^n} \frac{\mathbf{u}^{n+3/4} - \mathbf{u}^{n+2/4}}{\triangle t} \cdot \mathbf{v}\, d\mathbf{x} + \frac{\mu}{2} \int_{\Omega^n} \boldsymbol{\nabla} \mathbf{u}^{n+3/4} : \boldsymbol{\nabla} \mathbf{v}\, d\mathbf{x} - \\
&\quad \int_{\Omega^n} p^{n+3/4} \boldsymbol{\nabla} \cdot \mathbf{v}\, d\mathbf{x} = -\frac{\mu}{2} \int_{\Omega^n} (\boldsymbol{\nabla} \mathbf{u}^{n+2/4})^t : \boldsymbol{\nabla} \mathbf{v}\, d\mathbf{x} \quad \forall\, \mathbf{v} \in \mathbf{V}_0^n, \\
&\int_{\Omega^n} q\, \boldsymbol{\nabla} \cdot \mathbf{u}^{n+3/4}\, d\mathbf{x} = 0, \quad \forall\, q \in L^2(\Omega^n).
\end{aligned} \tag{62}$$

Update the position of the free surface by solving

$$\begin{aligned}
&\frac{\partial \eta}{\partial t} + u_1^{n+3/4} \frac{\partial \eta}{\partial x_1} = u_2^{n+3/4}, \quad \text{for } x_1 \in [0, L),\ t \in (t^n, t^{n+1}), \\
&\eta(x_1, t^n) = \eta^n(x_1), \\
&\eta(0, t) = \eta(L, t),\ \forall t \in (t^n, t^{n+1}),
\end{aligned} \tag{63}$$

and define η^{n+1} as the regularization of $\eta(t^{n+1})$ obtained by the projection onto the space of the H^1–periodic functions defined on $[0, L]$.

With the new free boundary described by η^{n+1}, we define the new domain Ω^{n+1} by mapping the *reference domain* $\tilde{\Omega} = (0, L) \times (0, H)$ onto the new domain using the bijective transformation $\mathbf{F} : \tilde{\Omega} \longrightarrow \Omega^{n+1}$, $(x_1, x_2) = \mathbf{F}(\xi_1, \xi_2)$ defined by

$$\begin{aligned} x_1 &= \xi_1, \\ x_2 &= \xi_2 \frac{\eta^{n+1}(\xi_1)}{H}. \end{aligned} \tag{64}$$

So, in the last fractional step, we "transport" $\mathbf{u}^{n+3/4}$ from Ω^n to Ω^{n+1} to obtain $\mathbf{u}^{n+1}$. More precisely, we define $\mathbf{u}^{n+1}$ on Ω^{n+1} from $\mathbf{u}^{n+3/4}$ (defined on Ω^n) as

$$\mathbf{u}^{n+1}(x_1, x_2) = \mathbf{u}^{n+3/4}\left(x_1, x_2 \frac{\eta^n(x_1)}{\eta^{n+1}(x_1)}\right) = \mathbf{u}^{n+3/4}\left(\xi_1, \xi_2 \frac{\eta^n(\xi_1)}{H}\right), \tag{65}$$

with ξ_1 and ξ_2 given by the inverse transformation of the one defined by (64).

Remark 6 *In the above formulation we have decoupled the two velocity components from the deformation tensor using the property*

$$\int_{\Omega(t)} \mathbf{D}(\mathbf{u}) : \mathbf{D}(\mathbf{v})\, d\mathbf{x} = \frac{1}{2}\int_{\Omega(t)} \boldsymbol{\nabla}\mathbf{u} : \boldsymbol{\nabla}\mathbf{v}\, d\mathbf{x} + \frac{1}{2}\int_{\Omega(t)} (\boldsymbol{\nabla}\mathbf{u})^t : \boldsymbol{\nabla}\mathbf{v}\, d\mathbf{x}, \ \forall\, \mathbf{v} \in \mathbf{V}_0(t),$$

and evaluated the second integral with the velocity at the previous splitting step, obtaining a significant simplification from the computational point of view.

3.3 Finite Element Approximation

At time t^n the domain Ω^n is non–polygonal, because of the curved free boundary γ^n. We here use an isoparametric version (discussed in, e.g., [21] Chapter 5) of the finite element method used in [10], where P_1 *iso* P_2 and P_1 finite element approximations are used to approximate the velocity field and pressure, respectively. Suppose that $\mathcal{T}_h$ is a triangulation of Ω^n and that it has been decomposed as $\mathcal{T}_h = \mathcal{T}_{0h} \bigcup \mathcal{T}_{1h}$ where

$$\mathcal{T}_{0h} = \{T | T \in \mathcal{T}_h,\ T \textit{ has two vertices on } \partial\Omega^n \textit{ and their related edge is curved}\}, \tag{66}$$

$$\mathcal{T}_{1h} = \{T | T \in \mathcal{T}_h,\ \textit{the three edges of } T \textit{ are rectilinear}\}. \tag{67}$$

Every curved triangle $T \in \mathcal{T}_{0h}$ is approximated by the quadrilateral $\tilde{T}$ defined by a_{1T}, a_{2T}, a_{23T}, a_{3T}, where a_{23T} is the mid–point of the arc defined by (a_{2T}, a_{3T}), or an approximation of this mid–point, as shown in Figure 6. The quadrilateral $\tilde{T}$ is decomposed in four sub–triangles K_{iT}, $i = 1, 2, 3, 4$, and we define the six–dimensional space

$$\tilde{P}_2(T) = \{q \mid q \in \mathcal{C}^0(T),\ q|_{K_{iT}} \in P_1 \ \ \forall\, i = 1, 2, 3, 4\}, \tag{68}$$

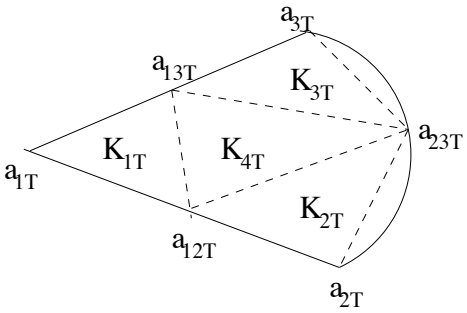

Figure 6: Approximation of a curved triangle T by $\tilde{T} = \bigcup_{i=1}^{4} K_{iT}$.

and the three–dimensional subspace of $\tilde{P}_2(T)$

$$\tilde{P}_1(T) = \{q \mid q \in \tilde{P}_2(T),\ q(a_{ijT}) = \frac{q(a_{iT}) + q(a_{jT})}{2},\ \forall\, 1 \le i, j \le 3,\ i \ne j\}, \quad (69)$$

where P_1 denotes the space of polynomials of degree ≤ 1. We use above the convention $a_{ijT} = a_{jiT},\ \forall\, i,\ j,\ i \ne j$. Of course, if $T \in \mathcal{T}_{1h}$, then $\tilde{T} = T$, and therefore $\tilde{P}_2(T)$ and $\tilde{P}_1(T)$ are still defined as before. Let Ω_h^n be the interior of the union of all quadrilaterals and rectilinear triangles, then we define the pressure and velocity finite element spaces as

$$P_h^n = \{q_h \mid q_h \in \mathcal{C}^0(\overline{\Omega}_h^n),\ q_h|_T \in P_1,\ \forall\, T \in \mathcal{T}_{1h},\ q_h|_{\tilde{T}} \in \tilde{P}_1(T),\ \forall\, T \in \mathcal{T}_{0h}\}, \quad (70)$$

$$V_h^n = \{\mathbf{v}_h \mid \mathbf{v}_h \in (\mathcal{C}^0(\overline{\Omega}_h^n))^2,\ \mathbf{v}_h|_T \in (\tilde{P}_2(T))^2,\ \forall\, T \in \mathcal{T}_{1h},\ \mathbf{v}_h|_{\tilde{T}} \in (\tilde{P}_2(T))^2,\ \forall\, T \in \mathcal{T}_{0h}\}, \quad (71)$$

respectively. We just incorporate periodicity to define the discrete analogues of the spaces V_0^n and $\mathbf{W}_-^{n+1/4}$ on Ω_h^n that we denote by V_{0h}^n and $\mathbf{W}_{h-}^{n+1/4}$, respectively. Concerning the pressure we introduce $L^2_{P_h^n}$ defined (with obvious notation) by:

$$L^2_{P_h^n} = \{q_h | q_h \in P_h^n, q_h \text{ periodic at } x_1 = 0 \text{ and } x_1 = L\}.$$

Then, the fully discrete problem reads as follows:

Find $\mathbf{u}_h^{n+1/4} \in \mathbf{V}_{0h}^n$ and $p_h^{n+1/4} \in L^2_{P_h^n}$ such that

$$\rho \int_{\Omega_h^n} \frac{\mathbf{u}_h^{n+1/4} - \mathbf{u}_h^n}{\triangle t} \cdot \mathbf{v}_h \, d\mathbf{x} + \frac{\mu}{2} \int_{\Omega_h^n} \boldsymbol{\nabla} \mathbf{u}_h^{n+1/4} : \boldsymbol{\nabla} \mathbf{v}_h \, d\mathbf{x} - \int_{\Omega_h^n} p_h^{n+1/4} \boldsymbol{\nabla} \cdot \mathbf{v}_h =$$
$$s \int_{\gamma_h^n} \mathcal{H}(\eta_h^n)\, \mathbf{n} \cdot \mathbf{v}_h \, d\gamma_h^n + \int_{\Omega_h^n} \mathbf{g} \cdot \mathbf{v}_h \, d\mathbf{x} - \frac{\mu}{2} \int_{\Omega_h^n} (\boldsymbol{\nabla} \mathbf{u}_h^n)^t : \boldsymbol{\nabla} \mathbf{v}_h \, d\mathbf{x},\ \forall\, \mathbf{v}_h \in \mathbf{V}_{0h}^n, \quad (72)$$
$$\int_{\Omega_h^n} q_h \, \boldsymbol{\nabla} \cdot \mathbf{u}_h^{n+1/4} \, d\mathbf{x} = 0,\ \ \forall\, q_h \in L^2_{P_h^n}.$$

Compute $\mathbf{u}_h^{n+2/4}$ via the solution of the following advection problem on $\Omega_h^n \times (t^n, t^{n+1})$

$$\begin{aligned}
&\int_{\Omega_h^n} \frac{\partial \mathbf{u}_h}{\partial t} \cdot \mathbf{v}_h \, d\mathbf{x} + \int_{\Omega_h^n} (\mathbf{u}_h^{n+1/4} \cdot \boldsymbol{\nabla}) \mathbf{u}_h \cdot \mathbf{v}_h, d\mathbf{x} = 0, \ \forall \mathbf{v}_h \in \mathbf{W}_{h-}^{n+1/4}, \\
&\mathbf{u}_h(t^n) = \mathbf{u}_h^{n+1/4}, \\
&\mathbf{u}_h(t) = \mathbf{u}_h^{n+1/4}(t) \text{ on } \Gamma_{h-}^{n+1/4} \times (t^n, t^{n+1}), \\
&\text{and set } \mathbf{u}_h^{n+2/4} = \mathbf{u}_h(t^{n+1}).
\end{aligned} \tag{73}$$

Next, find $\mathbf{u}_h^{n+3/4} \in \mathbf{V}_{0h}^n$ and $p_h^{n+3/4} \in L^2_{P_h^n}$ so that

$$\begin{aligned}
&\rho \int_{\Omega_h^n} \frac{\mathbf{u}_h^{n+3/4} - \mathbf{u}_h^{n+2/4}}{\triangle t} \cdot \mathbf{v}_h \, d\mathbf{x} + \frac{\mu}{2} \int_{\Omega_h^n} \boldsymbol{\nabla} \mathbf{u}_h^{n+3/4} : \boldsymbol{\nabla} \mathbf{v}_h \, d\mathbf{x} - \int_{\Omega_h^n} p_h^{n+3/4} \boldsymbol{\nabla} \cdot \mathbf{v}_h = \\
&\quad - \frac{\mu}{2} \int_{\Omega_h^n} (\boldsymbol{\nabla} \mathbf{u}_h^{n+2/4})^t : \boldsymbol{\nabla} \mathbf{v}_h \, d\mathbf{x}, \quad \forall \mathbf{v}_h \in \mathbf{V}_{0h}^n, \\
&\int_{\Omega^n} q_h \, \boldsymbol{\nabla} \cdot \mathbf{u}_h^{n+3/4} \, d\mathbf{x} = 0, \quad \forall q_h \in L^2_{P_h^n}.
\end{aligned} \tag{74}$$

Update the position of the free surface by solving

$$\begin{aligned}
&\frac{\partial \eta_h}{\partial t} + u_{1h}^{n+3/4} \frac{\partial \eta_h}{\partial x_1} = u_{2h}^{n+3/4}, \ x_1 \in [0, L), \ t \in (t^n, t^{n+1}), \\
&\eta_h(x_1, t^n) = \eta_h^n(x_1), \\
&\eta_h(0, t) = \eta_h(L, t), \quad t \in (t^n, t^{n+1}),
\end{aligned} \tag{75}$$

and define η_h^{n+1} as the solution of this problem.

$$\text{Find the new discrete domain } \Omega_h^{n+1}, \tag{76}$$

by using the analogous transformation to (64) with η_h^{n+1}.

$$\text{“Transport” } \mathbf{u}_h^{n+3/4} \text{ from } \Omega_h^n \text{ to } \Omega_h^{n+1}, \tag{77}$$

to obtain $\mathbf{u}_h^{n+1}$ on Ω_h^{n+1}, in a similar way as in (65).

Remark 7 *The boundary integrals $s \int_\gamma \mathcal{H}(\eta) \, \mathbf{n} \cdot \mathbf{v} \, d\gamma$ in (72) are evaluated in the following way:*

$$\int_\gamma \mathcal{H}(\eta) \, n_1 \, v_1 \, d\gamma = - \int_0^L \left(1 + \left| \frac{\partial \eta}{\partial x_1} \right|^2 \right)^{-1/2} \frac{\partial v_1}{\partial x_1} \, dx_1, \tag{78}$$

$$\int_\gamma \mathcal{H}(\eta) \, n_2 \, v_2 \, d\gamma = - \int_0^L \frac{\partial \eta}{\partial x_1} \left(1 + \left| \frac{\partial \eta}{\partial x_1} \right|^2 \right)^{-1/2} \frac{\partial v_2}{\partial x_1} \, dx_1. \tag{79}$$

where $\mathbf{v} = \mathbf{v}(x_1, \eta(x_1))$ is periodic at $x_1 = 0$ and $x_1 = L$. These integrals contain only first order derivatives, then low–order basis functions (first order in the present case) can be used for their approximation.

Remark 8 *Problems like (75) are solved using a second order Taylor–Galerkin discretization on* $[0, L) \times (t^n, t^{n+1})$*, namely*

$$\int_0^L (\eta^{n+1} - \eta^n)\,\phi\; dx_1 = \triangle t \int_0^L \left(u_2 - u_1 \frac{\partial \eta^n}{\partial x_1} \right) \phi\; dx_1 - \frac{1}{2} \triangle t^2 \int_0^L u_1 \frac{\partial u_2}{\partial x_1} \phi\; dx_1 - \frac{1}{2} \triangle t^2 \int_0^L u_1 \frac{\partial \eta^n}{\partial x_1} \left(\frac{\partial u_1}{\partial x_1} \phi + u_1 \frac{\partial \phi}{\partial x_1} \right) dx_1. \tag{80}$$

where the integrals are approximated using linear piecewise polynomial functions associated to the velocity finite element space. That is, we use the vertices of the isoparametric approximation of velocity at the free surface γ^n*.*

Remark 9 *At every time step we map a regular mesh from the reference domain* $\tilde{\Omega} = (0, L) \times (0, H)$ *onto the new discrete domain* Ω_h^{n+1} *using the bijective transformation (64) with* η_h^{n+1} *instead of* η^{n+1}*.*

The *saddle–point systems* (72) and (73) are solved by an *Uzawa/conjugate gradient algorithms*, discussed in [20] and [24]. The pure advection problem (73) is solved by a *wave–like equation* method discussed in [17] and [51] (see also [21], Chapter 6).

4 Sedimentation of circular bodies in a Newtonian incompressible fluid

In this section we consider the numerical simulation of the sedimentation of circular rigid bodies in a rectangular cavity $\Omega \in R^2$ filled with a incompressible Newtonian viscous fluid. The main goal of these experiments is to validate or cross–validate the methodology described in Section 2, as we compare the numerical results obtained when the Taylor–Hood and Bercovier–Pironneau finite element approximations are used in the simulation. An important part of the computational experiments is the simulation of particle–fluid interaction as well as particle/particle and particle/wall collisions.

4.1 Sedimentation of a circular disk

We simulate the fall of a rigid circular disk in a two–dimensional bounded cavity filled with an incompressible Newtonian viscous flow. Simulating the impact of the disk with the bottom boundary of the cavity is part of the computational experiments.

The computational domain is the rectangular cavity $\Omega = (0, 2) \times (0, 6)$, and the circular disk has density $\rho_1 = 1.5$ and diameter 0.25. The fluid density is $\rho_f = 1.0$, and its viscosity is $\mu = 0.01$. At time $t = 0$, the body is located at $(1, 4)$, and released from rest under the action of gravity. The discretization parameters used in the computational experiments are $\Delta t = 0.001$, and the velocity mesh size $h = 1/64$ and $h = 1/128$ when the Taylor–Hood and Bercovier–Pironneau finite element approximations are used, respectively.

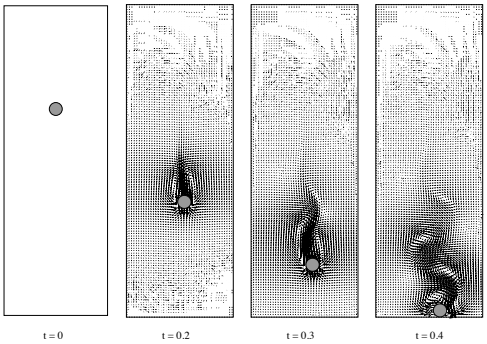

Figure 7: Particle position and flow visualization. Bercovier–Pironneau approximation.

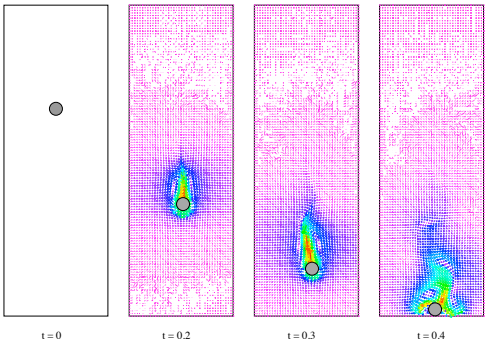

Figure 8: Particle position and flow visualization. Taylor–Hood approximation.

On Figures 7 and 8 we have visualized the particle position and associated flow (vector velocity field) at times $t = 0$, $t = 0.2$, $t = 0.3$ and $t = 0.4$, obtained with the Bercovier–Pironneau and Taylor–Hood finite element approximations, respectively. Figure 9 shows a comparison of the time histories of the x_1–coordinate and x_2–coordinate of the center of the disk, and of the horizontal and vertical components of its translational velocity. The above figures show that, in practice, the disk quickly reaches a uniform falling velocity until it hits the bottom of the cavity, and that a *symmetry breaking* takes place with the disk moving slightly on the right, away from the vertical symmetric axis of the cavity. The computed results show that there is a good agreement for the two finite element approximations. In particular, the maximum particle Reynolds number ($Re_p = \rho_1 \, 0.25 \, max|V_y|/\mu$) obtained is 452.1 for the Bercovier–Pironneau approximation and 466.8 for the Taylor–Hood approximation, which is a quite good quantitative agreement considering we are dealing with a highly nonlinear phenomenon involving symmetry breaking. Actually, in a previous result

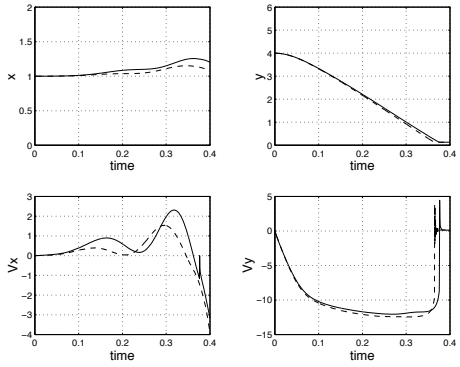

Figure 9: Histories of the x_1 and x_2 coordinates of the center of the disk (top figures). Histories of the horizontal and vertical coordinates of the translational velocity (bottom figures). Solid line: Bercovier–Pironneau approximation. Dashed line: Taylor–Hood approximation.

reported in [30] for this experiment with discretization parameters $h = 1/384$ and $\Delta t = 0.0005$ and the Bercovier–Pironneau approximation a maximum Reynolds number of 466 was found, which agrees very well with the result above obtained by the Taylor–Hood approximation. Further information concerning the computer implementation of the methods to solve these kind of problems can be found, e.g., [21] and [30].

4.2 Sedimentation and interaction of two circular disks

The objective of this test problem is to simulate the motion and interaction of two identical rigid circular disks sedimenting in a vertical channel. The two disks are initially at rest on the axis of the channel with a distance between their centers of one disk diameter. We expect the simulations to reproduce the well documented *drafting, kissing and tumbling* phenomenon. This fundamental phenomenon for Newtonian incompressible viscous flows has been observed in laboratory experiments and also via simulations based on computational methods different from those used here (see, for instance, [19], [63]).

Figures 10 and 11 shows the motion of two circular particles of density $\rho_1 = \rho_2 = 1.5$, falling in an incompressible viscous fluid of density $\rho_f = 1.0$ and viscosity $\mu = 0.01$. The computational domain is $\Omega = (0, 2) \times (0, 6)$, and the diameter of the particles is 0.25. The circular particles are released from rest with centers initially at $(1, 4.5)$ and $(1, 5)$, respectively. The simulations were performed with a time step $\triangle t = 0.001$ in both cases. The size of the velocity meshes were $h = 1/128$ and $h = 1/64$, when the Bercovier–Pironneau and Taylor–Hood approximations were applied, respectively. In both figures the *drafting, kissing and tumbling* phenomenon is clearly observed. The accepted explanation of this phenomenon is as follows:

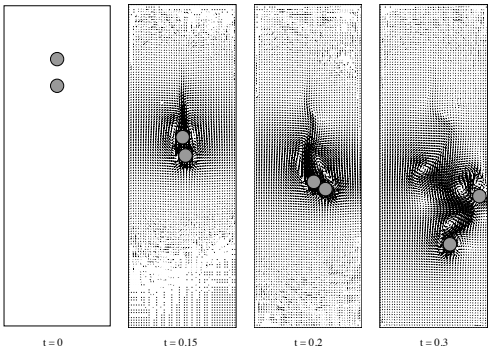

Figure 10: Disks positions and flow visualization (Bercovier–Pironneau approximation).

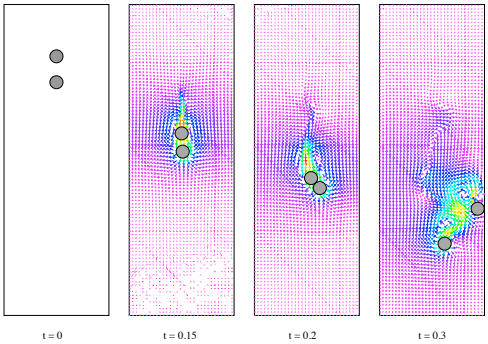

Figure 11: Disks positions and flow visualization (Taylor–Hood approximation).

The lower disk, when falling, creates a pressure drop in its wake. This implies (if close enough) that the upper disk encounters less resistance (drag) from the fluid than the lower one and settles faster. Falling faster, the upper disk "*kisses*" the lower one. Once in contact or near contact, the two disks act as an *elongated body* falling in an incompressible viscous fluid. As well known, elongated bodies falling sufficiently fast in a Newtonian incompressible viscous fluid have a tendency to *rotate* so that their broad side becomes perpendicular to the main flow direction. Indeed rotation takes place, as seen in figures 10, 11, at t = 0.2, but such two disks' assemble is unstable and the two disks separate.

Figure 12 shows a comparison of the time evolution of the x_1 and x_2–coordinates of the center of mass of the two disk, and of their translational velocities (V_1, V_2). Figure 13 shows the time history of the separation distance between the two disks. The maximum particle Reynolds numbers based on maximum falling velocity are 677.7 and 706.5 obtained from the Bercovier–Pironneau and Taylor–Hood approximations, respectively. Considering that the

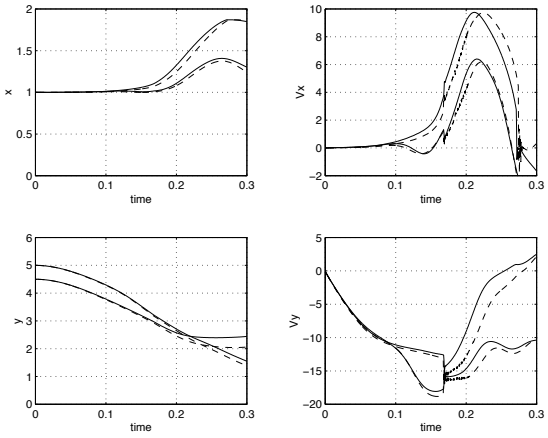

Figure 12: Histories of the x_1 and x_2 coordinates of the centers of the disks (left figures). Histories of the horizontal and vertical coordinates of the translational velocities (right figures). Solid line: Bercovier–Pironneau approximation. Dashed line: Taylor–Hood approximation.

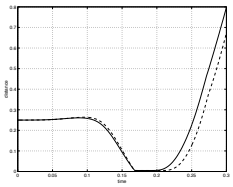

Figure 13: History of the distance between the two disks. Solid line: Bercovier–Pironneau approximation. Dashed line: Taylor–Hood approximation.

dynamics is pretty fast and that the *drafting, kissing and tumbling* phenomenon is pretty violent (see Fig. 12), the qualitative and quantitative agreement between the computed results for the two approximations is quite good. Further information about the results presented here can be found in [21], [30], [40].

4.3 Sedimentation and interaction of 100 circular disks

As last test problem with circular particles we consider the falling motion of 100 circular disks in a Newtonian incompressible viscous fluid in a two dimensional cavity. This problem differs from the previous ones in that the number of particles is much larger. Indeed this test problem can be viewed as a *particulate flow* problem, and the computational method method discussed in Section 2 still apply to this more complicated situation. In fact, results for the sedimentation of 6400 disks in a two–dimensional cavity and

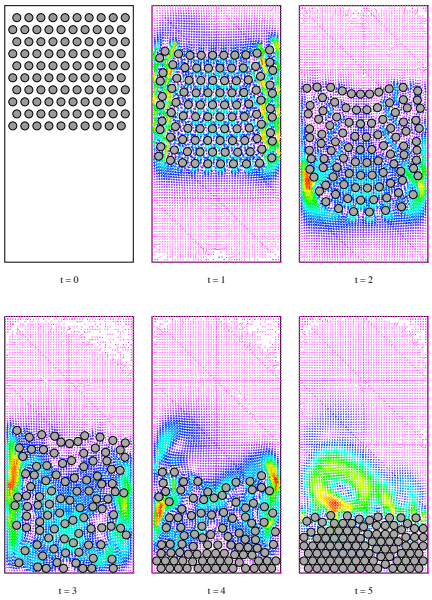

Figure 14: Disks positions and flow visualization. Taylor–Hood approximation.

fluidization of 1204 spherical particles in a three–dimensional tube (bed) have been obtained applying the same methodology and reported in see [52] and [53], respectively. Those experiments were performed using the Bercovier–Pironneau finite element approximation, because for these problems where many particle "move around" a fine (uniform) mesh is required essentially everywhere, so that *fast Poisson solvers* and *fast elliptic solvers* based in *cyclic reduction methods* [32] are very convenient to solve these linear problems. The two and three–dimensional discrete Poisson and elliptic problems obtained in the discretization of those problems were solved using the package FISHPACK (see [2]). For the cases where the Taylor–Hood approximation were used, we applied a sparse matrix algorithm based on Markowitz' method (Pissanetzky (1984)), requiring more memory to storage these matrices, however we were able to solve the sedimentation problem of as many as 504 particles in a two–dimensional cavity ([40]), but the time of computation increases quit a lot.

Figure 14 shows the sedimentation and interaction of 100 disks of density $\rho_j = 1.01$, $j = 1, ..., 100$, in an incompressible viscous fluid of density $\rho_f = 1.0$ and viscosity $\mu = 0.01$. The computational domain is a closed channel with dimensions $\Omega = (0, 1) \times (0, 2)$, and the diameter of the disks is 0.0625. The solid fraction in this test case is 15.34%. The particles are released from rest with the initial arrangement shown in Figure 2 at $t = 0$. These results were obtained by the Taylor–Hood approximation. At $t = 1$ and $t = 2$ we can observe that the particles at the center of the channel fall faster than the other and the liquid close the left and right walls is displaced to the vertical upper direction. Between $t = 2$ and $t = 4$ a complicated recirculation phenomenon occurs and at $t = 5$ almost all particles are settled at the bottom of the channel. Knowing that problems with with many particles may exhibit a chaotic–like behavior where instabilities may develop into many symmetry breaking and other bifurcation phenomena, including *drafting, kissing, and tumbling* taking place at various scales and times, this time we compare averages of the quantities describing the dynamical behavior of the mixture. We solved the problem with the Bercovier–Pironneau approximation and compared the results with the previous solution. Figure 15 shows a comparison of the time history of the average x_1 and x_2 coordinates of the centers of the 100 disks and their average velocity, obtained by the two methods. Again the agreement is satisfactory.

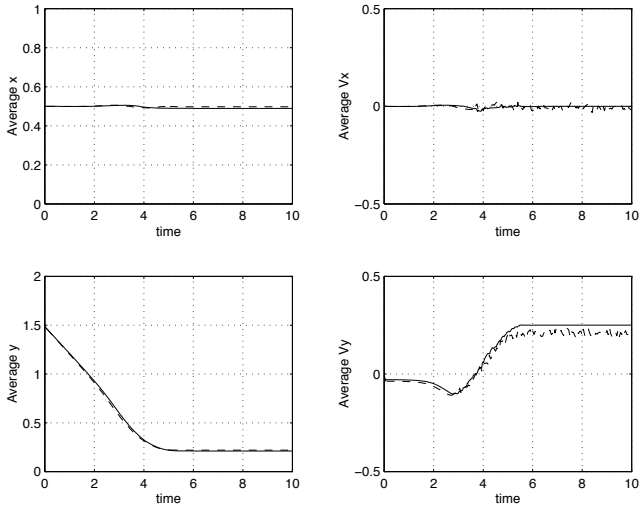

Figure 15: Histories of the average x_1 and x_2 coordinates of the centers of the 100 disks (left figures). Histories of the horizontal and vertical coordinates of the translational average velocity of the 100 disks (right figures). Solid line: Bercovier–Pironneau approximation. Dashed line: Taylor–Hood approximation.

5 Sedimentation of non–circular bodies in a Newtonian incompressible fluid

One of the principal goals of these simulations is to check numerically the well–known fact that when an elongated rigid body sediments in a Newtonian incompressible fluid of sufficient small viscosity, it will rotate until its broad side becomes horizontal. The numerical results shown in this section were obtained using the methodology described in Section 2, and the pair $\{\mathbf{u}, p\}$ has been approximated using the Taylor–Hood discrete velocity and pressure described in Section 2.4. We consider two cases with elongated bodies: an elliptic body, and a two–disk cluster. As a last example in this section, we include the numerical simulation of the motion of an *tripole–like rigid body* (three–disk cluster) falling in a Newtonian incompressible viscous fluid. This interesting example shows how the distribution of mass and added moment of inertia, compared to a simple cylinder (circular or elliptic), plays a significant role on the particle–fluid interaction.

5.1 Sedimentation of an elliptic rigid body

We first consider the motion of an elliptic body, of density $\rho_1 = 1.25$, falling in a Newtonian incompressible viscous fluid of density $\rho_f = 1.0$, and viscosity $\mu = 0.1$. The computational domain is the rectangular cavity $\Omega = (0, 2) \times (0, 6)$, and the lengths of the major and minor axes of the ellipse are 0.5 and 0.25, respectively. The body is released from rest with its center at $(1, 4)$ and its broad side in the vertical direction ($\phi^0 = \pi/2$). The simulation was performed with a mesh size $h = 1/32$ and time step $\triangle t = 0.001$. The results shown in this section were first published in [38] and [21].

The sedimentation of this elliptic body and the associated flow is visualized in Figure 16. Initially, the body moves vertically without rotation, then it starts to rotate in the counterclockwise direction before it reaches its maximum vertical velocity. The maximal Reynolds number of the flow (relative to the the length of the major axis) is 45.27. Figures 16 and 17 show that this rotation is quite sudden. As the elliptic body rotates it approaches the right wall, and its falling velocity decreases dramatically due to the stronger drag force acting on the rotated body. The higher stress on the right hand side of the body when it is close to the wall due to lubrication forces, prevent the body to touch that right wall, and it finally sediments on the bottom with its broad side horizontal.

We also computed the flow when the elliptic body is released from rest with its broad side horizontal. This time the body sediments as shown in Figure 18. At first glance, it seems that the body broadside stays horizontal during the sedimentation. However Figure 19 shows small oscillations around the center of mass, and small oscillating deviations from the symmetry vertical axis of the cavity Ω. The body touches the bottom boundary at about $t = 0.78$, and the maximum Reynolds number is 28.1. We observe also that the settling velocity is essentially uniform for $t \in (0.4, 0.6)$.

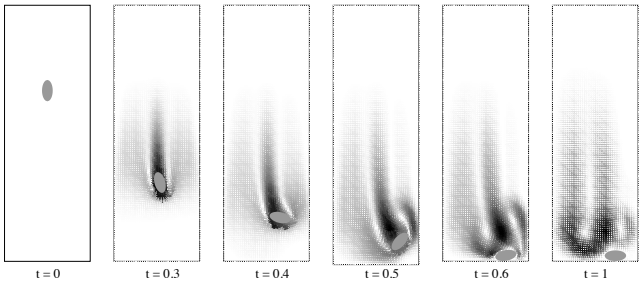

Figure 16: An elliptic body falling in a viscous fluid from a vertical initial position.

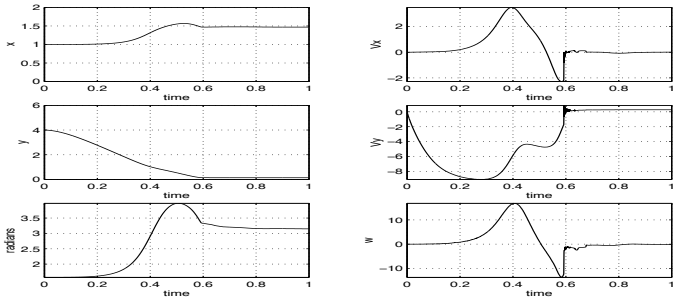

Figure 17: Histories of the x_1 and x_2 coordinates of the center of the elliptic body, and of the rotation angle (left figures). Histories of the horizontal and vertical coordinates of the translational velocity of the elliptic body, and of the angular velocity (right figures).

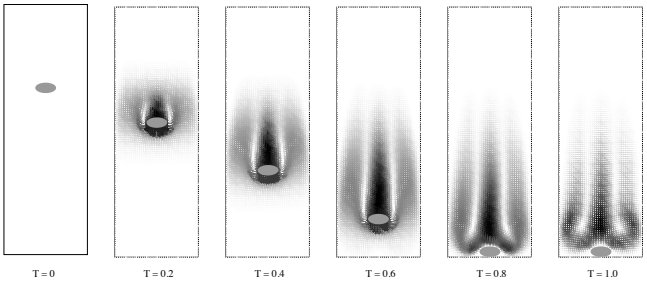

Figure 18: A elliptic horizontal body falling in a viscous fluid.

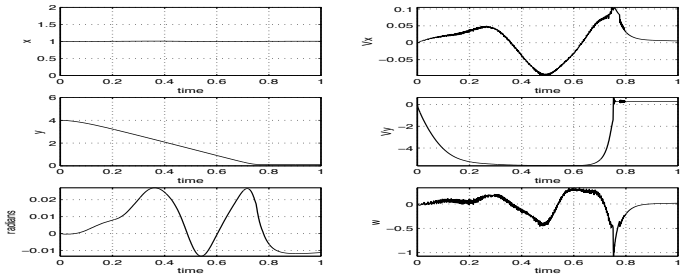

Figure 19: Histories of the x_1 and x_2 coordinates of the center of the elliptic body, and of the rotation angle (left figures). Histories of the horizontal and vertical coordinates of the translational velocity of the elliptic body, and of the angular velocity (right figures).

5.2 Sedimentation of a two–disk cluster

We consider the direct numerical simulation of the sedimentation of a two–disk cluster in the rectangular cavity $\Omega = (0, 2) \times (0, 6)$ filled with a Newtonian incompressible viscous fluid; the falling body is thus non–convex and its boundary contains two cusps. This experiment has some similarity with the *drafting, kissing, and tumbling* phenomenon discussed before. Indeed in this phenomenon the two bodies form for a short while the two–body cluster very similar to the one considered here. Also, this experiment has some similarities with the experiment of the sedimentation of a elliptic body, as we will see below. The numerical results shown below can be found in [21].

The cluster under consideration consists of two identical disks of diameter 0.25, rigidly attached to each other, forming thus an elongated non–convex body of length 0.5. The fluid and solid characteristics are the same as in the case of the sedimentation of the elliptic body: $\rho_f = 1$, $\rho_1 = 1.25$, $\mu = 0.1$, the fluid being Newtonian and incompressible. The same mesh and finite element approximation are used as in the previous experiment, and we still have $\triangle t = 0.001$. At time $t = 0$ the fluid and the rigid are at rest, with the center of mass of the two–disk cluster located at $(1, 4)$.

For the first simulation, we assumed that the broadside of the cluster is vertical. The sedimentation of the body and the corresponding flow is visualized in Figure 20, while on Figure 21 we have represented the time variation of the horizontal and vertical displacements of the center of mass, of the angle rotation, and of the corresponding velocities. The maximum Reynolds number of the fluid flow in this case is 44.1.

For the second simulation, we assume that at time $t = 0$, the broadside of the two–disk cluster is horizontal, everything else being the same. Figure 22 suggests that the broadside stays horizontal during the sedimentation, but a close look at Figure 23 suggests that the falling body suffers small oscillations around its center the mass, and small oscillating deviations from the symmetry vertical

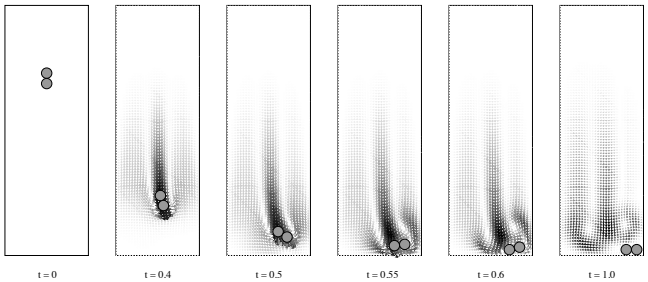

Figure 20: Sedimentation of a two–disk cluster in a two–dimensional cavity filled with a Newtonian incompressible viscous fluid.

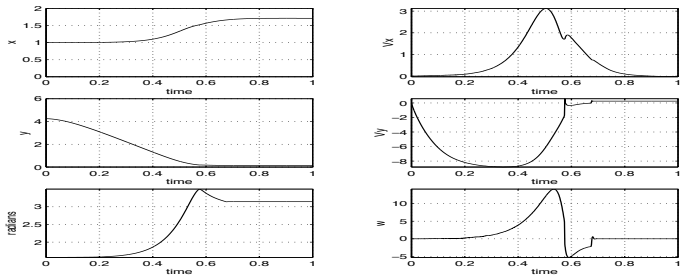

Figure 21: Histories of the x_1 and x_2 coordinates of the center of the two–disk cluster, and of the rotation angle (left figures). Histories of the horizontal and vertical coordinates of the translational velocity of the elliptic body, and of the angular velocity (right figures).

axis of the cavity Ω. On the other hand, the settling velocity is essentially uniform for $t \in (0.4, 0.6)$ and the maximum Reynolds number of the fluid flow is 31. The body touches the bottom boundary of Ω about $t = 0.8$.

We want to conclude this section by calling attention to the remarkable similarities between the settling of the elliptic body and the settling of the two–disk cluster. This is clear observing Figures 16, 20, and Figures 18, 22, as well as Figures 17, 21, and Figures 19, 23.

5.3 Sedimentation of a tripole–like body

In this section we consider the direct numerical simulation of the motion of a tripole–like rigid body ([41]), of density $\rho_1 = 1.25$, falling in a Newtonian incompressible viscous fluid of density $\rho_f = 1.0$, and viscosity $\mu_f = 0.01$. The computational domain is $\Omega = (0, 2) \times (0, 12)$, and the lengths of the cylinders' diameter that form the tripole–like rigid body is 0.25. As before the body is non–convex, but this time its boundary contains six cusps. The body is released

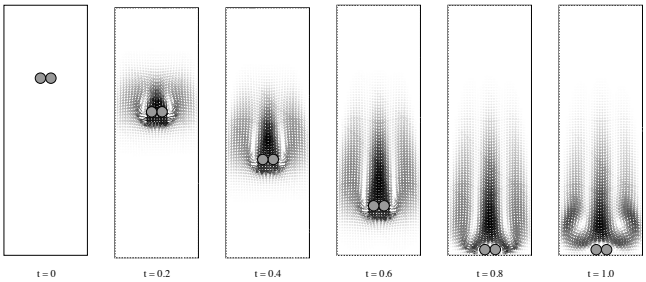

Figure 22: Sedimentation of an horizontal two–disk cluster in a two–dimensional cavity filled with a Newtonian incompressible viscous fluid.

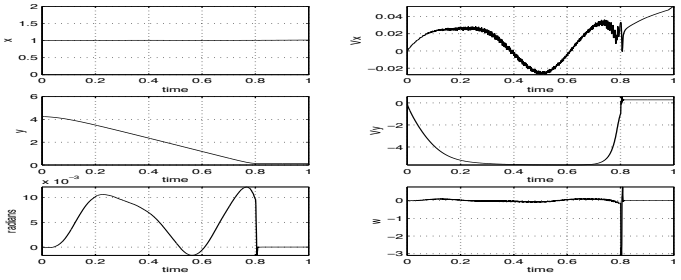

Figure 23: Histories of the x_1 and x_2 coordinates of the center of the two–disk cluster, and of the rotation angle (left figures). Histories of the horizontal and vertical coordinates of the translational velocity of the elliptic body, and of the angular velocity (right figures).

from rest with its center at $(1, 11.5)$, and its leading cylinder (yellow) is placed horizontally facing the right hand side wall ($\phi^0 = 0$). The simulation was performed using the Taylor–Hood finite element approximation with a mesh size $h = 1/32$ and time step $\triangle t = 0.001$. The sedimentation of the tripole–like body and the associated flow is shown in Figure 24. The velocity flow field is described by the black arrows and the pressure field is described by color contour plots. Red indicates the highest pressure and purple the lowest pressure in this RGB scale. Actually, only the hydrodynamical pressure is shown, since the hydrostatic pressure is so strong that there is not a significant difference between highest and lowest pressures.

Due to its initial orientation, the rigid body starts to rotate almost immediately in the clockwise direction. While falling down the body drifts to the left until it "touches" the left wall. At this time (t = 0.44) the orientation of the rigid is symmetrically similar to the initial orientation, and after separation from the wall it rotates again in the clockwise direction, so that it approaches the same wall one more time. This time (t= 0.83) the body touches the wall with the leading cylinder ahead, and after separating from the wall it starts to rotate in the opposite direction (counterclockwise). The rigid body then drifts to the right and approaches the right wall. Before touching the right wall the rigid body sediments with its leading cylinder on top and with the other two cylinders touching the bottom. The strong recirculation behind the body causes the body to move to the left after it reaches the bottom. Figure 24 shows a sequence of vortices generated by the motion of rigid body in the fluid. The Reynolds number based on terminal vertical velocity is about 404, and it hits the bottom boundary at $t = 1.8$ This shows that the motion of the body depends on more than the flow field around it. Apparently the direction of rotation of the rigid body is more associated with the distribution of mass and the added moment of inertia than to the hydrodynamical forces and torques. However, it is clear that the hydrodynamical forces on the system with the initial conditions chosen are responsible for the initial symmetry breaking which starts the rotation. A more detailed description of motion of the rigid body is shown in Figure 25 which shows the histories of the position (x_1, x_2, ϕ) and velocity (V_1, V_2, ω) of the rigid body. The oscillatory behavior of the horizontal and vertical translation velocity is associated to the wake structure behind the body, while the angular velocity behavior is more associated to the moment of inertia of the body.

6 Flow past elliptic bodies in a two–dimensional channel

Here we present numerical results concerning flow past elliptic bodies in a two–dimensional channel. We include the case of a flow past a freely rotating two–dimensional elliptic body with its center fixed at the centerline of the channel. This study was motivated by previous results ([42]) concerning the direct simulation of freely rotating cylinders in viscous flows by a methodology entirely different to the one used here. As a second example problem, we

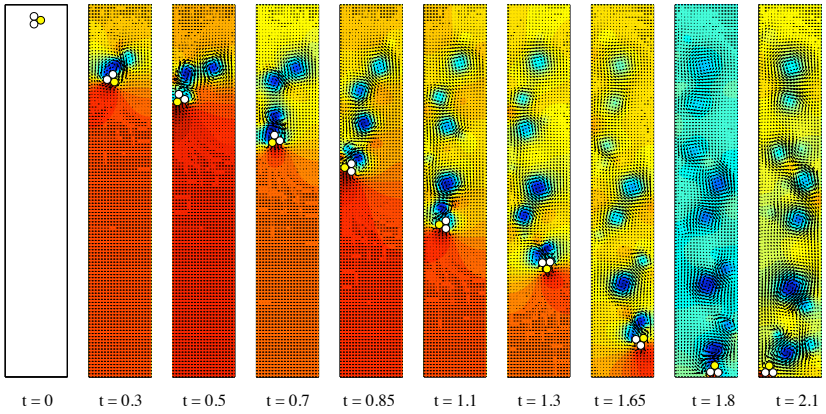

Figure 24: A tripole–like body falling in a viscous fluid.

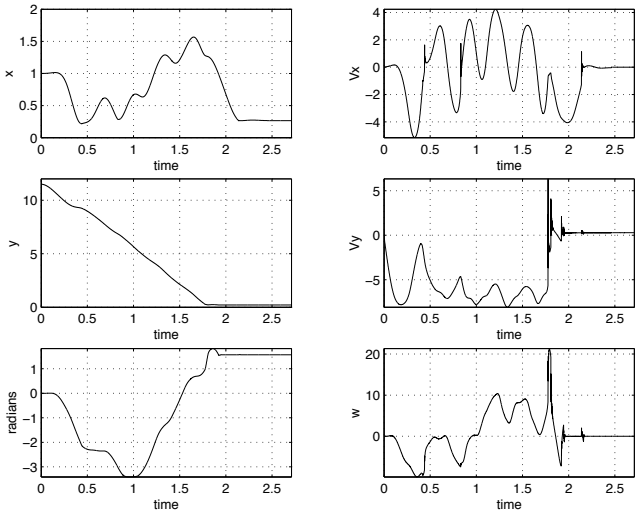

Figure 25: Histories of the x_1 and x_2 coordinates of the center of the rigid body, and of the rotation angle (left figures). Histories of the horizontal and vertical coordinates of the translational velocity of the rigid body, and of the angular velocity (right figures).

present the numerical results of the free motion of a elliptic pendulum in an incompressible viscous fluid. More details can be found in [23].

6.1 Freely rotating two–dimensional elliptic body

We consider the flow past a freely rotating two–dimensional elliptic body in the channel $\Omega = (-15, 40) \times (-4, 4)$ filled with a viscous incompressible liquid of density $\rho_f = 1$. The flow is assumed to move from left to right, and acts on a rigid elliptic body of density $\rho_1 = 1.1$, with center fixed at $(0, 0)$. The lengths of the major and minor axes of the elliptic body are $a = 1$ and $b = 0.5$, respectively. The motion of the body is described by its angular position θ (defined as the the angle of the major axes with the horizontal), and its angular velocity $\omega = d\theta/dt$. Thus $\frac{d\mathbf{V}}{dt} = \mathbf{0}$, $\mathbf{g} = \mathbf{0}$ and $\mathbf{F}_1^r = \mathbf{0}$ in model (1)–(8). This problem is solved for Reynolds numbers $Re = 20$, 100 and 200. The Reynolds number is defined as $Re = \rho_f U a/\mu$, where U is the maximum inlet velocity at the upstream boundary. As initial conditions we choose $\theta^0 = 0$, $\omega^0 = 0$, and $\mathbf{u}^0 = \mathbf{0}$. These problems are solved applying the Bercovier–Pironneau approach on a non–regular mesh, with refinement in the region where the ellipse rotates, as shown in Figure 26(a). The collocation points inside the elliptic body as well as the collocation points chosen on its boundary are shown in Figure 26(b). The time step is $\triangle t = 0.001$ for all cases. For these meshes we are unable to use the fast elliptic solvers. Instead we use a sparse matrix algorithm based on Markowitz' method [57].

For $Re = 20$ the elliptic body rotates counterclockwise so that its broad side tends to be perpendicular to the flow direction, as qualitatively expected [38]. The flow tends to a steady state and the elliptic body remains in its stable vertical position $\theta = \pi/2$, as shown in Figs. 27 and 28. For $Re = 100$ and 200 unsteady oscillatory solutions are obtained. The main feature of these solutions is periodic oscillation of the elliptic rigid body around its vertical position, as shown in Figures 29 and 31. These oscillations are associated with vortex shedding behind the elliptic body (see Figures 30 and 32). Both, the amplitude of the oscillations and the angular velocity of the elliptic body, are larger at higher Reynolds number. Concerning the frequency, it is a common practice to find the Strouhal number defined as $St = 2fa/U$, where f is the frequency of the oscillations, and U and a are defined as before. For the cases considered here we obtain $St = 0.19$ and $St = 0.22$ for $Re = 100$ and $Re = 200$,

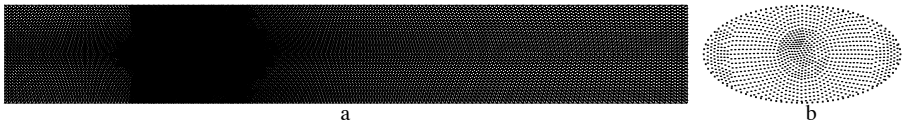

Figure 26: (a) Non–regular mesh for the velocity. (b) Collocation points: mesh nodes inside the elliptic rigid body and points chosen on its boundary.

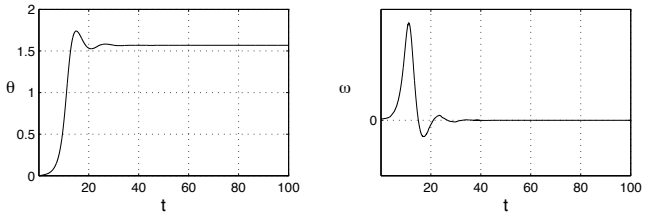

Figure 27: Time history of the angle and of angular velocity of the ellipse. $Re = 20$.

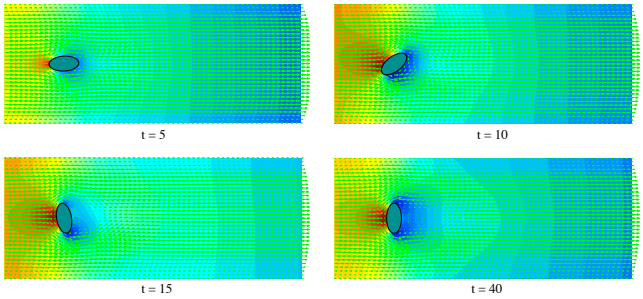

Figure 28: Visualization of the pressure and velocity vector field at different times. $Re = 20$.

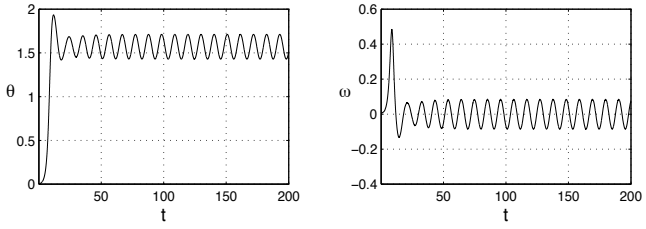

Figure 29: Time history of the angle and of angular velocity of the ellipse. $Re = 100$.

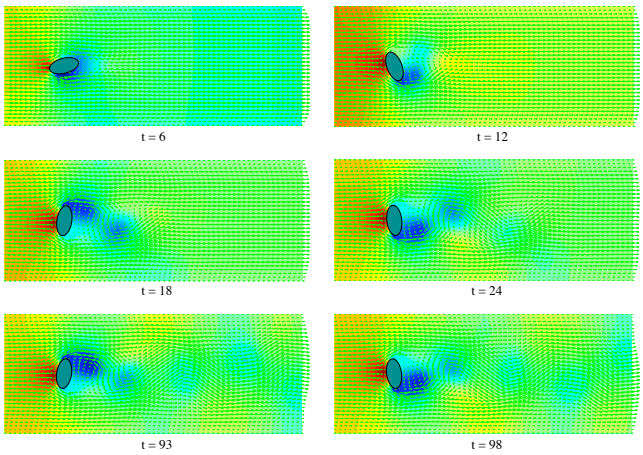

Figure 30: Visualization of the pressure and velocity vector field at different times. $Re = 100$.

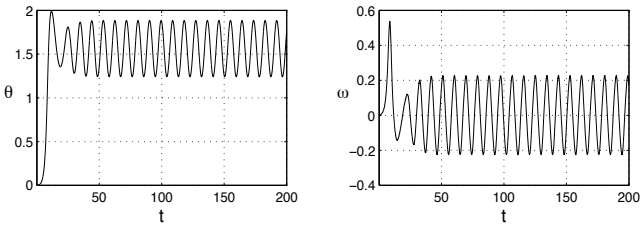

Figure 31: Time history of the angle and of angular velocity of the ellipse. $Re = 200$.

respectively. These results are consistent with previous results about a freely rotating cylinder in a channel [42].

6.2 Hydrodynamic elliptic pendulum

Here we present the results of the free motion of a elliptic pendulum in an incompressible viscous fluid. The hydrodynamic elliptic pendulum is defined in the following way: the center **G** of the elliptic rigid body is constrained to move on a circular trajectory around the fixed axis of rotation **O**, as shown in Figure 33; simultaneously the elliptic body rotates freely around its center **G**. This pendulum is placed in a channel where the flow direction is from left to right. The position and orientation of the elliptic body are known at any time by the angles θ and ϕ, respectively. The velocity of the rigid body is known through the angular velocities $\omega = d\theta/dt$ and $\zeta = d\phi/dt$. The elliptic body has the same dimensions as in the previous examples. The axis of rotation of

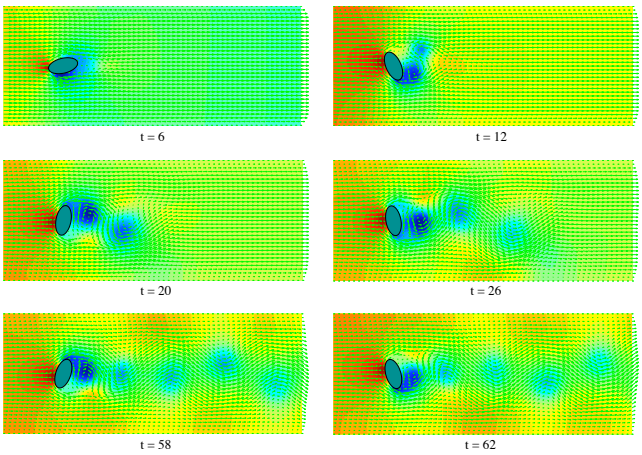

Figure 32: Visualization of the pressure and velocity vector field at different times. $Re = 200$.

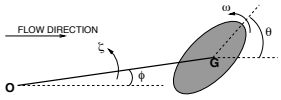

Figure 33: A pendulum with a free to rotate elliptic body in a viscous fluid.

the pendulum is located at $\mathbf{O} = (-8, 0)$, and the length of the pendulum is $l_p = |\overrightarrow{\mathbf{OG}}| = 8$. Equations (1)–(8) are simplified using the constraint relation $\frac{d\mathbf{V}}{dt} = \zeta\, l_p\, (-sin\phi, cos\phi)$, and $\mathbf{g} = \mathbf{0}$, $\mathbf{F}_1^r = \mathbf{0}$. The initial conditions are $\theta^0 = 0$, $\phi^0 = 0$, $\omega^0 = 0$, $\zeta^0 = 0$, and $\mathbf{u}^0 = \mathbf{0}$. We solve the problem for $Re = 200$, where Re is defined as before. The main feature of the solution is periodic oscillation of the pendulum around its axes $\mathbf{O}$ coupled with periodic oscillation of the elliptic body around its center $\mathbf{G}$, as shown in Figure 34. The amplitude of rotation of the rigid body around its center is about fifteen times larger than the amplitude of rotation of the pendulum for this particular case. In fact, we expect that the longer l_p the shorter the amplitude of oscillation of the pendulum [64]. These oscillations have the same frequency as the oscillations of the free to rotate elliptic body for $Re = 200$ (see Figure 31). This corroborates that the oscillations are strongly associated with vortex shedding behind the elliptic body. The result is a synchronized periodic motion of both the pendulum and body. Figure 35 shows, at different times, some snapshots of the pressure and velocity vectors in a region near the body. However, a distinctive characteristic of the solution here is that that the amplitude of rotation and angular velocity of the elliptic body around its center $\mathbf{G}$ are significantly higher than those obtained for a freely rotating elliptic body placed at the center of the channel.

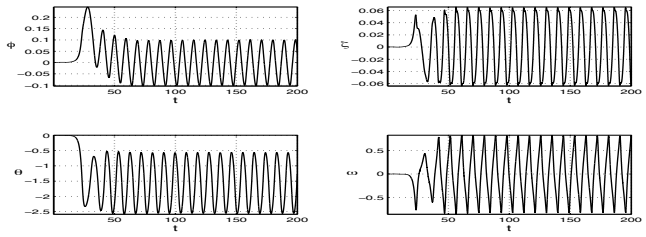

Figure 34: Time history of the angle and angular velocity of the pendulum (top), and of the angle and angular velocity of the elliptic rigid body (bottom) at $Re = 200$.

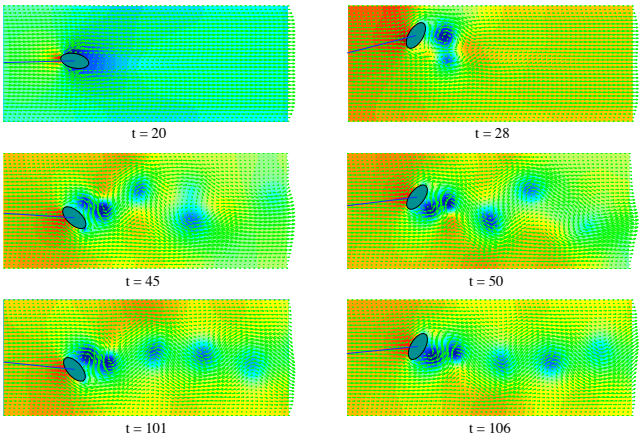

Figure 35: Visualization of the pressure and velocity vector field at different times. Hydrodynamic pendulum, $Re = 200$.

This phenomenon is due to the unsymmetrical shear, produced by the presence of the channel walls, on the two sides of the elliptic body when it is off the center line of the channel. When the elliptic body moves up the higher shear on the upper part of the body introduce a net rotation (in addition to the induced rotation by vortex shedding) in the clockwise direction, while when it moves down the body gets an additional net rotation in the counterclockwise direction. Again this is consistent with previous results found in [34] and [42].

7 Hydrodynamic circular pendula under the action of gravity

In this section we consider the numerical simulation of the motion of pendula in a Newtonian incompressible viscous fluid. The pendula are circular cylinders

constrained to move in a circular trajectory as shown in Figure 36. The motion of the cylinders are driven only by the hydrodynamical forces and gravity.

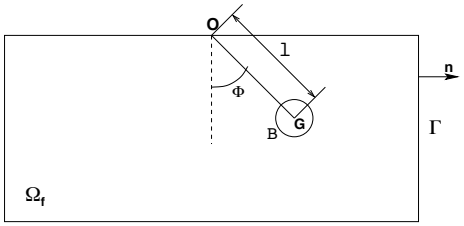

Figure 36: Pendulum in a viscous fluid under the action of gravity

In the present calculations we allowed solid surfaces to touch and penetrate, contrary to what was done in previous work. In fact, a good feature of the methodology described in Section 2 is that the numerical solution does not break down when the rigid bodies overlap. On the other hand, numerical methods in which the computational domain is remeshed may break down when collision occurs, because this would break the lattice modeling of the fluid [34]. Hence a repulsive force between the particles need to be incorporated when they are close to each other to prevent contact between surfaces. We did not introduce these artificial repulsive forces here, in part because we wanted to investigate the solutions when the rigid bodies are near collision or when they actually collide and overlap. The mechanics of how solid particles in viscous liquids stick or rebound has not been fully understood and is still subject of current research. It has been demonstrated theoretically that when a perfect rigid sphere approaches a rigid wall its kinetic energy is dissipated by non–conservative viscous forces. The rate of close approach is asymptotically slow and the sphere do not deform or rebound [14]. By simultaneously accounting for elastic deformation of the body and viscous fluid forces, Davis *et al.* [16] showed that part of the incoming particle kinetic energy is dissipated by fluid forces and internal solid friction, and the rest is transformed into elastic–strain energy of deformation. Depending on the fraction of the kinetic energy that becomes stored as elastic–strain energy, the deformation of the spheres may be significant and rebound may occur. The relevant parameter for the bouncing transition, which is often obtained experimentally [37], is the *Stokes number*, which characterize the particle inertia relative to viscous forces. Numerical results of colliding bodies in viscous fluids may help to understand the mechanics of individual collisions in solid–liquid flows, which is an important issue in particulate multi–phase flow modeling and in the actual numerical computations of these flows. An interesting study of pendula in viscous fluids with some applications can be found in [64] and references therein.

The numerical experiments in this work include the motion of a single pendulum, and the motion of two pendula in a two–dimensional rectangular domain $\Omega = (-3, 3) \times (-1, 1)$ filled with a viscous fluid of density $\rho_f = 1$. The axis of rotation of the pendula is fixed at $\mathbf{O} = (0, 1)$, and the diameter of the

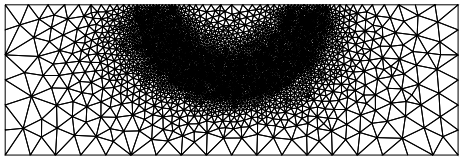

Figure 37: The unstructured mesh

circular rigid bodies is 0.25 in all cases bellow. The two pendula case include different numerical experiments where the disks may have different densities and initial positions. Equations (1)–(8) are simplified by introducing the constraint relation $\mathbf{V} = \boldsymbol{\omega} \times \overrightarrow{\mathbf{GO}} = l\,\omega\,(cos\phi,\, sin\phi)$, and $\mathbf{F}_j^r = \mathbf{0}$. The Taylor–Hood finite element approximation was applied to these problems.

7.1 One pendulum

As a test case we consider one pendulum with a circular rigid body of density $\rho_1 = 3$ released from rest at $\phi^0 = 1.4$ radians in a liquid of viscosity $\mu = 0.005$. We solved this problem using two meshes: an unstructured mesh (Fig. 37) which takes advantage of the fact that we know in advance the possible trajectory of the rigid body, and a uniform mesh with space discretization step $h = 1/64$. Figure 38 shows the comparison of the time history of the angle and of the angular velocity obtained with the two meshes. The agreement is satisfactory.

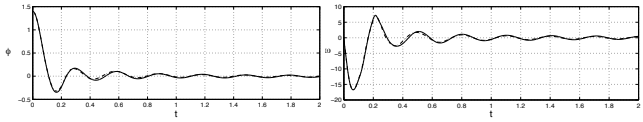

Figure 38: Comparison of the time history of the angle (left) and of the angular velocity (right) obtained with the unstructured mesh (dashed line) and the regular mesh (continuous line) for one pendulum

As expected, the pendulum exhibits damped oscillations around the vertical position, and it goes to a steady position as time increases. The maximum Reynolds number obtained (based on the maximum falling velocity and diameter of the circular rigid body) was 835. Since the unstructured mesh has much less velocity degrees of freedom than the regular mesh (13823 versus 49665), we used the unstructured mesh in the subsequent calculations.

7.2 Two pendula

As a second example we consider two pendula. One pendulum with a circular rigid body of density $\rho_1 = 1.1$ is initially hold in the vertical position $\phi_1^0 = 0$, and the other pendulum with density $\rho_2 = 5$ is released from rest at $\phi_2^0 = 1.4$ radians in a liquid of viscosity $\mu = 0.005$. Figure 39 shows that, after a

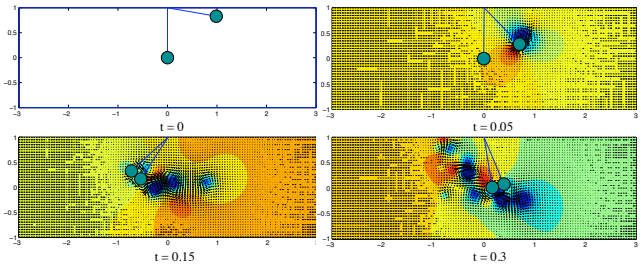

Figure 39: Velocity vector field and pressure at different times for the two pendula with $\mu_f = 0.005$, $\rho_1 = 1.1$, and $\rho_2 = 5$.

short time, the heavier cylinder collides with the lighter fixed body. After collision the two bodies move together as a single body all the time. This is more evident in in Figure 40 where the time history of the angle, angular velocity, and separation distance is shown. The maximum Reynolds number in this case was 1,085. We expected the two bodies to separate after they reach the maximum negative angle since the heavier rigid body is below to the lighter one at that position, and the action of gravity is stronger on the heavier body. However they never separate after collision. The only forces in our model problem that can prevent separation after collision are the viscous forces which in this case seem to dominate. To corroborate this strong dependence from viscous effects, we reduced the viscosity μ from 0.005 to 0.001 and repeated the numerical calculation. Figure 41 shows that this time, after the two bodies collide, they stick together until they reach the maximum negative angle (where the angular velocity is close to zero), and then separate when they start to move in the counterclockwise direction by the action of gravity. This is clearly shown in Figure 42 where we plot the time history of angle, angular velocity, and separation distance. The maximum Reynolds number this time was 5,800. It is evident that a more detailed study of this and related phenomena is needed in order to better understand the mechanics of particle collision in viscous liquids and to generate models that simulate more accurately solid–liquid particulate flows which are very important in applications.

8 Numerical simulation of a fluid flow with a free capillary surface

We want to conclude this article by including the numerical results of the Navier–Stokes equations modeling incompressible viscous fluid flow with a capillary free–surface, obtained by applying the methodology described in Section 3. For a more detailed description of this methodology and of the numerical results see [22].

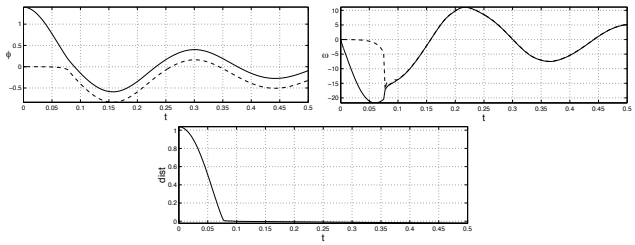

Figure 40: Time history of the angle (top left), angular velocity (top right), and separation distance (bottom) of the two pendula with $\mu_f = 0.005$, $\rho_1 = 1.1$, and $\rho_2 = 5$.

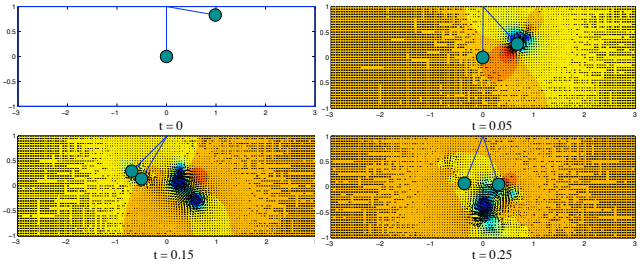

Figure 41: Velocity vector field and pressure at different times for the two pendula with $\mu_f = 0.001$, $\rho_1 = 1.1$, and $\rho_2 = 5$.

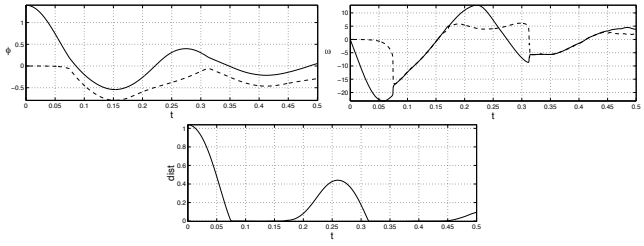

Figure 42: Time history of the angle (top left), angular velocity (top right), and separation distance (bottom) of the two pendula with $\mu_f = 0.001$, $\rho_1 = 1.1$, and $\rho_2 = 5$.

8.1 Perturbed flow in an horizontal periodical plane

As a first example we consider the situation where a liquid of viscosity $\mu = 0.01$ and density $\rho = 1$, occupies a periodic region in the plane, resting on an horizontal line. The liquid is initially at rest but the free surface on top is not in equilibrium. The surface tension coefficient is $s = 1$, and $H = 1$, $L = 1$. The initial non–equilibrium position of the free surface is shown in Figure 46. The discretization parameters are $h_p = 1/40$ to approximate the pressure, so that $h_v = 1/80$ for the approximation of velocity and the free surface, and $\triangle t = 0.00025$. For $t > 0$ the coupled action of gravity and surface tension produces a motion which leads to the equilibrium state $\eta = 1$ and $\mathbf{u} = \mathbf{0}$ through an oscillating regime. Figure 43 shows the velocity fluid field and color isobars of the pressure. Figure 44 shows the position of the free surface at different times. We observe that the flow and the free boundary shape have a qualitative behavior very similar to the one shown in [4], where the simulation of a fluid flow in a three–dimensional annular container is considered.

8.2 Perturbed flow in an inclined periodical plane

As a second example, we consider the flow of a liquid of viscosity $\mu = 0.1$, density $\rho = 1$, and surface tension coefficient $s = 1$, in an 45 degrees inclined periodic plane. To simplify the geometry, and still employ the methodology in Section 5.1, we keep Ω as above and give the gravity vector a 45^o inclination. In this frame we choose $H = 1$, $L = 0.15$, and the initial non–equilibrium position of the free surface is similar as in the previous case and shown in Figure 46. This time we chose $h_p = 1/200$ to approximate pressure, so that $h_v = 1/400$ to approximate velocity and the free surface, and $\triangle t = 0.00025$. The velocity vector field and pressure (color) contours at different times are shown in Figure 45. The shape of the free surface at different times is shown in Figure 46. This time the equilibrium solution of the problem for velocity $\mathbf{u}$ is a Poiseuille distribution with $\mathbf{u} = \mathbf{0}$ only along the plane and maximum velocity taking place along $\eta = 0.15$. Computations done with a mesh twice coarser provide essentially the same results, suggesting that for $h_p = 1/200$ and $h_v = 1/400$ a pretty accurate solution has been obtained.

Acknowledgments

R. Glowinski and T.W. Pan acknowledge also the support of NSF (grants ECS-9527123, CTS-9873236, DMS-9973318, CCR-9902035, DMS-0209066), and DOE/LASCI (grant R71700K-292-000-99). Part of this work was done while L.H.J. was visiting the Department of Mathematics of the University of Houston. The hospitality of both Prof. R. Glowinski and Prof. T.W. Pan is gratefully acknowledged, as well as the finantial support from the University of Houston, Universidad Autónoma Metropolitana-I, and CONACyT (México). We acknowledge also Prof. Enrique Fernández–Cara for his invitation to write this article.

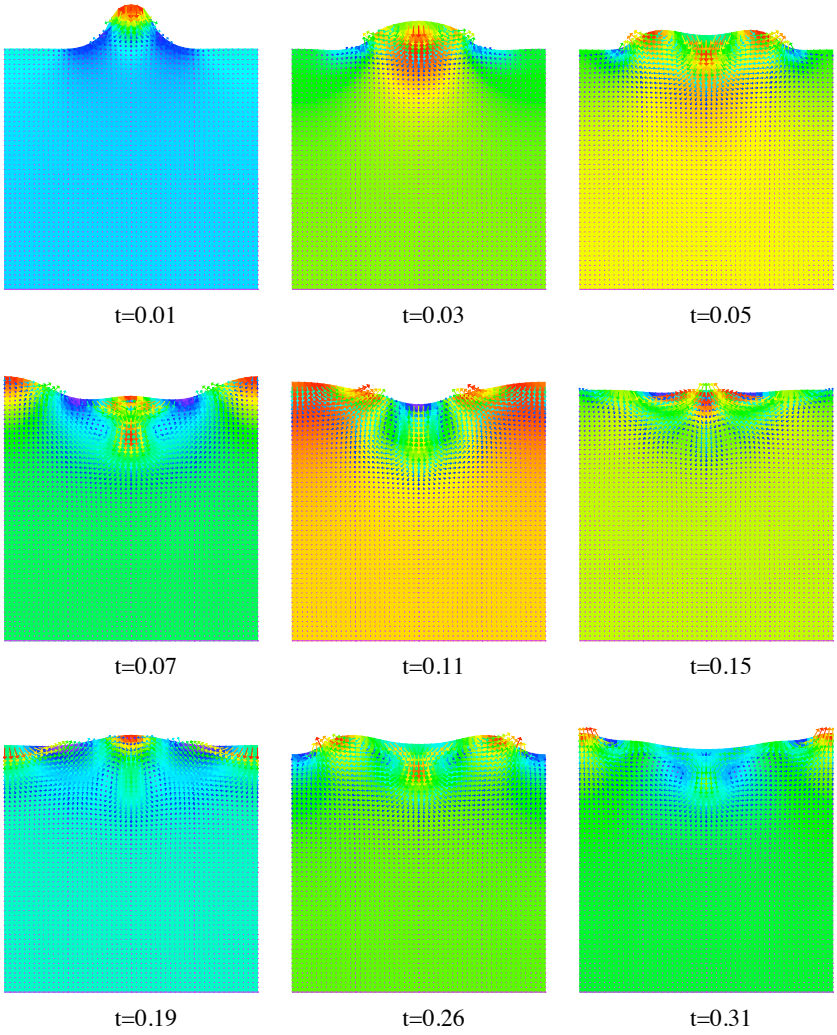

Figure 43: Velocity and pressure at different times for Example 1.

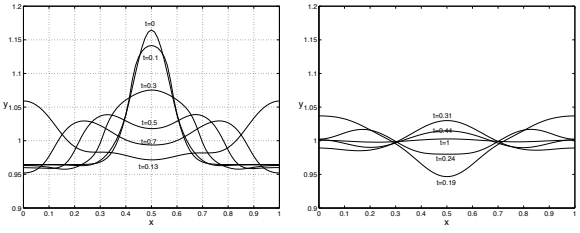

Figure 44: Position of the free surface at different times for Example 1.

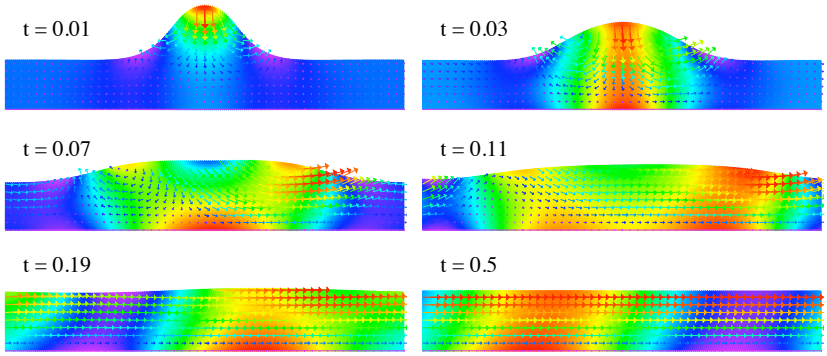

Figure 45: Velocity and pressure at different times for Example 2.

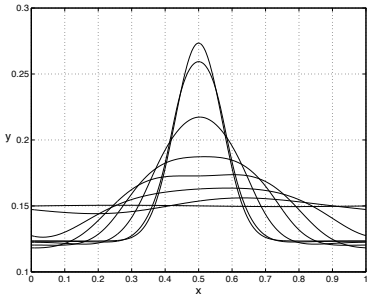

Figure 46: Position of the free surface at different times for Example 2. From top to bottom: t=0, 0.01, 0.03, 0.05, 0.07, 0.11, 0.19, 0.5.

References

[1] Y. Achdou and Y. Kuznetsov (1997). Algorithms for the mortar element method. In *Domain Decomposition Methods in Sciences and Engineering*, edited by R. Glowinski, J. Periaux, Z.C. Shi, O. Widlund, Wiley, Chichester, 33–42.

[2] J.P. Adam, P. Swarztrauber and R.A. Sweet (1980). FISHPACK: A package of Fortran subprograms for the solution of separable elliptic partial differential equations. Published by the *National Center for Atmospheric Research* (NCAR), Boulder, CO.

[3] G. Allain (1987). Small–time existence for the Navier–Stokes equations with a free surface, *Appl. Math. Optim.*, **16**, 37–50.

[4] E. Bänsch (2001). Finite element discretization of the Navier–Stokes equations with a free capillary surface. *Numer. Math.*, **88**, 203–235.

[5] E. Bänsch, and B. Hön (1999). Numerical simulation of a silicon floating zone with a free capillary surface. In *Scientific Computing in Chemical Engineering II*, edited by F. Keli, W. Mackens, H. Voss and J. Werther, **1**, 328–335.

[6] J.T. Beale (1981). The initial value problem for the Navier–Stokes equations with a free surface. *Comm. Pure Appl. Math.*, **34**(3), 359–392.

[7] J.T. Beale and A. Majda (1981). Rates of convergence for viscous splitting of the Navier–Stokes equations, *Math. Comput.*,**37**, 243–260.

[8] M. Bercovier and O. Pironneau (1979). Error estimates for the Finite Element Solution of the Stokes Problem in the Primitive Variables, *Numer. Math.*, **33**, 211–224.

[9] F. Bertrand, P.A. Tanguy and F. Thibault (1997). A three–dimensional fictitious domain method for incompressible fluid flow problem, *Int. J. Num. Meth. Fluids*, **25**, 719–736.

[10] M.O. Bristeau, R. Glowinski and J. Periaux (1987). Numerical methods for the Navier–Stokes equations. Application to the simulation of compressible and incompressible flows, *Computer Physics Report*, **6**, 73–188.

[11] A. J. Chorin (1967). A numerical method for solving incompressible viscous flow problems, *J. Comput. Phys.*, **2**, 12–26.

[12] A. J. Chorin (1968). Numerical solution of the Navier–Stokes equations, *Math. Comput.*, **23**, 341–354.

[13] A. J. Chorin (1973). Numerical study of slightly viscous flow, *J. Fluid Mech.*, **57**, 785–796.

[14] R.E. Cox and H. Brenner (1967). The slow motion of a sphere through a viscous fluid towards a plane surface II. Small gap widths including inertial effects, *Chem. Engng. Sci.*, **22**, 1753.

[15] C. Cuvelier and R. M. Schulkes (1990). Some numerical methods for the computation of capillary free boundaries governed by the Navier–Stokes equations, *SIAM Review*, **32**(2), 355–423.

[16] R.A. Davis, J.M. Serayssol and E.J. Hinch (1986). The elastohydrodynamic collision of two spheres, *J. Fluid Mech.*, **163**, 479–497.

[17] E.J. Dean and R. Glowinski (1997). A wave equation approach to the numerical solution of the Navier–Stokes equations for incompressible viscous flow, *C.R. Acad. Sci. Paris*, **325**, Série I, 789–797.

[18] E.J. Dean, R. Glowinski and T.W. Pan (1998). A wave equation approach to the numerical simulation of incompressible viscous fluid flow modeled by the Navier–Stokes equations. In *Mathematical and Numerical Aspects of Wave Propagation*, edited by J.A. De Santo, SIAM, Philadelphia, 65–74.

[19] J. Feng, H.H. Hu and D.D. Joseph (1994). Direct simulation of initial value problems for the motion of solid bodies in Newtonian fluid. Part 1. Sedimentation, *J. Fluid Mech.*, **261**, 95–134.

[20] M. Fortin and R. Glowinski (1983). *Augmented Lagrangian Methods*, North–Holland, Amsterdam.

[21] R. Glowinski (2003). *Finite Element Methods for Incompressible Viscous Flow* in P.G. Ciarlet and J.-L. Lions eds. Handbook of Numerical Analysis, Vol IX, North–Holland, Amsterdam, 3–1176.

[22] R. Glowinski and L. H. Juárez (2003). Finite element method and operator splitting for a time–dependent viscous incompressible free surface flow, *Comput. Fluid Dyn. J.*, **12**(3):55, 459–468.

[23] R. Glowinski, L. H. Juárez and T. W. Pan (2003). On the numerical simulation of incompressible viscous fluid flow around moving rigid bodies of elliptical shape. In *Numerical Simulation of Incompressible Flows*, edited by M. M. Hafez, World Scientific Pub. Co., Singapure, 179–202.

[24] R. Glowinski, and P. Le Tallec (1989). *Augmented Lagrangians and Operator Splitting Methods in Nonlinear Mechanics*, SIAM, Philadelphia.

[25] R. Glowinski, T. I. Hesla, D. D. Joseph and T.W. Pan (1997). Distributed Lagrange multiplier methods for particulate flow. In *Computational Science for the 21st Century*, edited by M.O. Bristeau, G.J. Etgen, W. Fitzgibbon, J. Périaux and M.F. Wheeler, Wiley, Chichester, 270–279.

[26] R. Glowinski, T. W. Pan, T. I. Hesla and D. D. Joseph (1999). A distributed Lagrange multiplier/fictitious domain method for particulate flow, *Int. J. of Multiphase Flow*, **25**, 5, 755–794.

[27] R. Glowinski, T.W. Pan, T.I. Hesla, D.D. Joseph and J. Periaux (1998). A fictitious domain method with distributed Lagrange multipliers for the numerical simulation of particulate flow. In *Domain Decomposition Methods 10*, edited by J. Mandel, C. Farhat and X.C. Cai, AMS, Providence, RI, 121–137.

[28] R. Glowinski, T.W. Pan, T.I. Hesla, D.D. Joseph and J. Periaux (1999). A distributed Lagrange multiplier/fictitious domain method for flows around moving rigid bodies: Application to particulate flow, *Int. J. Numer. Meth. Fluids*, **30**, 1043–1066.

[29] R. Glowinski, T.W. Pan, T.I. Hesla, D.D. Joseph and J. Periaux (2000). A distributed Lagrange multiplier/fictitious domain method for the simulation of flows around moving rigid bodies: Application to particulate flow, *Comput. Meth. Appl. Mech. Eng.*, **184**, 241–267.

[30] Glowinski, R., Pan, T. W., Hesla, T. I., Joseph, D. D. and Periaux, J. (2001). A Fictitious domain Approach to the Direct Numerical Simulation of Incompressible Viscous Flow Past Moving Rigid bodies: Application to Particulate Flow, *J. Comput. Phys.*, **169**, 363–426.

[31] R. Glowinski and O. Pironneau (1992). Finite element methods for the Navier–Stokes equations, *Annual Rev. Fluid Mech.*, **24**, 167–204.

[32] G.H. Golub, C. Van Loan (1996). *Matrix Computations*, 3rd. edition, Johns Hopkins University Press, Baltimore MD.

[33] K. Hofler, M. Muller, S. Schwarzer and B. Wachman (1998). Interacting particle–liquid systems. In *High Performance Computing in Science and Engineering*, edited by E. Krause, W. Jager, Springer–Verlag, Berlin, 54–64.

[34] H.H. Hu, D.D. Joseph and M. Crochet (1992). Direct Simulation of Fluid Particle Motion, *Theoret. Comput. Fluid Dynamics*, **3**, 285–306.

[35] H.H. Hu, N.A. Patankar and M.Y. Zhu (2001). Direct numerical simulation of fluid–solid systems using arbitrary Lagrangian–Eulerian techniques, *J. Comput. Phys.*, **169**(2), 427–462.

[36] A. Johnson and T. Tezduyar (1997). 3–D simulations of fluid–particle interactions with the number of particles reaching 100, *Comput. Methods Appl. Mech. Engrg.*, **145**, 301–321.

[37] G.G. Joseph, R. Zenit, M.L. Hunt and A.M. Rosenwinkel (2001). Particle–wall collision in a viscous fluid, *J. Fluid Mech.*, **433**, 329–346.

[38] L.H. Juarez (2001). Numerical Simulation of the Sedimentation of an Elliptic Body in an Incompressible Viscous Fluid, *C. R. Acad. Sci. Paris, Série IIb* **329**, 221–224.

[39] L.H. Juárez and R. Glowinski, (2001). Numerical simulation of the motion of pendula in an incompressible viscous fluid by Lagrange multiplier/fictitious domain methods. In *Domain Decomposition Methods in Science and Engineering*, edited by I. Herrera, D.E. Keyes, O.B. Widlund, R. Yates, UNAM, México.

[40] L.H. Juárez, R. Glowinski and T.W. Pan (2002). Numerical simulation of the sedimentation of rigid bodies in an incompressible viscous fluid by Lagrange multiplier/fictitious domain methods combined with the Taylor–Hood finite element approximation, *J. Sci. Comput.*, **17**(1–4), 683–694.

[41] L.H. Juárez, R. Glowinski and B.M. Pettitt, (2002). Numerical simulation of the sedimentation of a tripole–like body in an incompressible viscous fluid, *Appl. Math. Letters*, **15**, 743–747.

[42] H. Juarez, R. Scott, R. Metcalfe and B. Bagheri (2000). Direct Simulation of Freely Rotating Cylinders in Viscous Flows by High–order Finite Element Methods, *Comput. & Fluids*, **29**, 547–582.

[43] L.H. Juárez, P. Saavedra and M. Salazar (1994). Computational study of a free–boundary model. In *Advance in Optimization and Numerical Analysis*, edited by S. Gomes and J. P. Hennart, Kluwer Academic Publisher, The Netherlands, 245–260.

[44] J.B. Keller and M.J. Miksis (1983). Surface tension driven flows, *SIAM J. Appl. Math.*, **43**, 268–277.

[45] S.F. Kistler and L.E. Scriven (1984). Coating flow theory by finite element method and asymptotic analysis of the Navier–Stokes system. *Int. J. Numer. Methods Fluids*, **4**, 207–229.

[46] B. Maury (1999). Direct simulation of 2–D fluid–particle flows in biperiodic domains, *J. Comput. Phys.*, **156**, 325–351.

[47] B. Maury and R. Glowinski (1997). Fluid–particle flow: a symmetric formulation, *C.R. Acad. Sci. Paris, Série I*, **324**, 1079–1084.

[48] Marchuk, G. I. (1990). Splitting and alternate direction methods. In *Handbook of Numerical Analysis*, vol. 1, Ciarlet, P. G. and Lions, J. L. (eds.), North–Holland, Amsterdam, 197–462.

[49] J.A. Nietsche (1986). Free boundary problems for Stokes flows and finite element method, *Ecuadiff 6*, Lectures Notes in Math., vol. 1192, Springer Verlag, Berlin, 327–332.

[50] M. Padula and V.A. Solonnikov (2000). On Rayleigh–Taylor stability, *Ann. Univ. Ferrara–Sez. VII–Sc. Mat.*, vol XLVI, 307–336.

[51] T.W. Pan and R. Glowinski (2000). A projection/wave–like equation method for the numerical simulation of incompressible viscous fluid flow modeled by the Navier–Stokes equations, *Comput. Fluid Dyn. J.*, **9**(2), 28–42.

[52] T. W. Pan, D.D. Joseph and R. Glowinski (2001). Modeling Rayleigh–Taylor instability of a sedimenting suspension of several thousand circular particles in a direct simulation, *J. Fluid Mech.*, **434**, 23–37.

[53] T. W. Pan, D.D. Joseph, R. Bai and R. Glowinski (2002). Fluidization of 1204 spheres: Simulation and experiment, *J. Fluid Mech.*, **451**, 169–191.

[54] C.S. Peskin (1977). Numerical analysis of blood flow in the heart, *J. Comput. Phys.*, **25**, 220–252.

[55] C.S. Peskin and D.M. McQueen (1980). Modeling prosthetic heart valves for numerical analysis of blood flow in the heart, *J. Comput. Phys.*, **37**, 113–132.

[56] O. Pironneau (1989). *Finite Element Methods for Fluids*, (Wiley, Chichester).

[57] S. Pissanetsky, 1984. *Sparse Matrix Technology*, Academic Press.

[58] C. Pozrikidis (1988). The flow of a liquid film along a periodic wall, *J. Fluid Mech.*, **188**, 275.

[59] W.G. Pritchard (1986). Instability and chaotic behavior in a free–surface flow, *J. Fluid Mech.*. **165**, 1–60.

[60] W.G. Pritchard, R.L. Scott and S.J. Tavener (1992). Numerical and asymptotic methods for certain viscous free–surface flows, *Phil. Trans. R. Soc. London. A*, **340**, 1–45.

[61] V.V. Pukhnachëv (1982). Hydrodynamic free boundary problems, *Nonlinear Partial Differential Equations and their Applications*, Collège de France Seminar Volume III, Pitman, Boston, 301–308.

[62] G. Riskin and L.G. Leal (1984). Numerical Solution of free boundary problems in fluid mechanics, Parts 1–3, *J. Fluid Mech.*, **148**, 1–43.

[63] J.B. Ritz and J.P. Caltagirone (1999). A numerical continuous model for the hydrodynamics of fluid–particle systems, *Int. J. Numer. Meth. Fluids*, **30**, 1067–1090.

[64] Y. Roux, E. Rivoalen and B. Marichali (2000). Vibrations Induites d'un Pendule Hydrodynamique, *C. R. Acad. Sci. Paris, Série IIb*, **328**, 479–497.

[65] P. Saavedra and L.R. Scott (1991). Variational formulation of a model free–boundary problem, *Math. Comput.*, **57**, 451–475.

[66] H. Saito and L.E. Scriven (1981). Study of coating flow by the finite element method. *J. Comput, Phys*, **42**, 53–76.

[67] D. Schwabe (1988). Surface–tension–driven flow in crystal growth melts, *Crystal Growth, Properties and Applications 11*, Berlin Springer.

[68] V.A. Solonnikov (1982). On the Stokes equations in domains with non–smooth boundaries and on viscous incompressible flow wit a free surface, *Nonlinear Partial Differential Equations and their Applications*, Collège de France Seminar Volume III, Pitman, Boston, 340–423.

[69] C. Taylor, P. Hood (1973) A numerical solution of the Navier–Stokes equations using the finite element method. *Comput. & Fluids* **1**, 73–100.

[70] S. Turek (1999). *Efficient Solvers for Incompressible Flow Problems: An Algorithmic and Computational Approach*, Springer–Verlag, Berlin.